Analysis of the material composition and ionic conductivity of bismuth fluoride and barium tin fluoride and how these factors affect their application in fluoride-ion batteries

Master Thesis

Written by: Jonne van Zeijl
Supervised by: Pedro Braga Groszewicz

April 1, 2022

Abstract

In the coming energy transition, the availability of reliable and affordable energy storage will be of vital importance. Battery storage is a large factor in the energy storage sector, and current battery storage is dominated by lithium-based batteries. However, lately, alternatives to lithium have been given renewed attention, due to the insufficient abundance of lithium in the earth's crust and the promising theoretical aspects of these other types of batteries. Fluoride-based batteries, for example, have high theoretical capacities and are theorized to be very suitable for application in solid-state battery technology. Fluoride-based batteries have only been produced on a lab-scale relatively recently, with the first reversible solid-state fluoride-ion battery produced in 2011, and the first room temperature reversible fluoride-ion battery produced in 2018, yet interest in this technology has drastically increased over the past few years. The current main issues fluoride-ion batteries are running into are its poor cyclability, its low current densities, and its inability to meet the theoretical capacities. In this report, multiple facets of fluoride-ion batteries have been analyzed in an effort to improve on these characteristics. In particular a focus has been placed on two commonly used materials in fluoride-ion batteries: electrolyte $BaSnF_4$ and cathode material BiF_3. The ionic conductivity dependence on pressure was deduced for each material, with $BaSnF_4$ having its highest ionic conductivity at $\sim$280 MPa and BiF_3 having its highest ionic conductivity at $\sim$680 MPa. To test the effect of oxides in BiF_3, which form spontaneously when BiF_3 is exposed to air or humidity, various Bi-O-F compounds were synthesized and had their ionic conductivity measured. It was found that each of the compounds that contained oxygen had a drastically lower (factor 1,000-10,000) ionic conductivity than pure BiF_3. An attempt was also made to improve the ionic conductivity of BiF_3 by doping that material with SnF_2. BiF_3 doped with SnF_2 concentrations of 5-20% were synthesized, and had their ionic conductivity measured. It was found that the ionic conductivity was increased by dopant concentrations of 5% and 10%, with the material with 10% SnF_2 having the highest ionic conductivity, while the materials with 15% and 20% SnF_2 had a similar ionic conductivity to pure BiF_3. Symmetric fluoride-ion batteries were also produced, with BiF_3 as an electrode material and $BaSnF_4$ as an electrolyte material. The produced batteries reached charge and discharge capacities with values of at most only 30% of the values reported in literature. The batteries also had poor capacity retention over multiple charge-discharge cycles. Batteries were also produced using BiF_3 doped with 5% and 10% SnF_2 as an electrode material. These batteries had higher initial capacities but had even poorer capacity retention over subsequent cycles. It was however also found that the critical current density for the batteries had increased as a result of doping with SnF_2, allowing higher current densities to be applied to the batteries.

Contents

1 Introduction to the topic

The global transition from fossil fuels to renewable energy is heavily dependent on the possibility to effectively store energy. [37][24][84] In this industry, battery technology will play an important part.[55][34][91][24] Current battery technology largely makes use of lithium-ion batteries[13]. As seen in figure 1, 89% of all battery storage consists of lithium-ion batteries, in which the transport of a negatively charged electrode is offset by the transport of a positively charged Li^+-ion in the same direction[25]. However, global lithium reserves are likely insufficient for the global energy transition to fully rely on this technology.[26][35][73]. Figure 2 shows the abundance of the elements in the earths crust. Lithium has an abundance of 10^3 atoms per 10^6 Si atoms. [23] This is insufficient for the amount of electrochemical storage that is needed for the energy transition. Besides issues of abundance, lithium batteries also suffer from issues regarding safety[12] and costs[67][15]. Additional battery technologies that do not rely on lithium are needed.

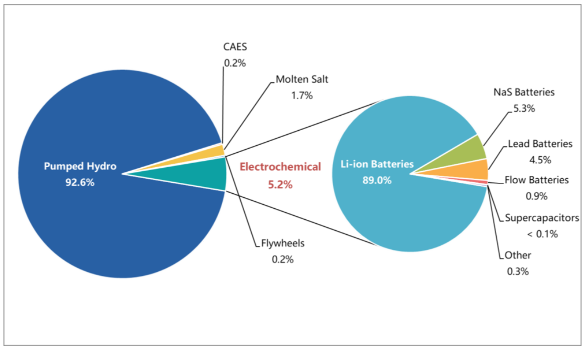

Figure 1: Current make-up of global energy storage. Note the dominance of lithium-ion battery technology within the battery storage section. [13]

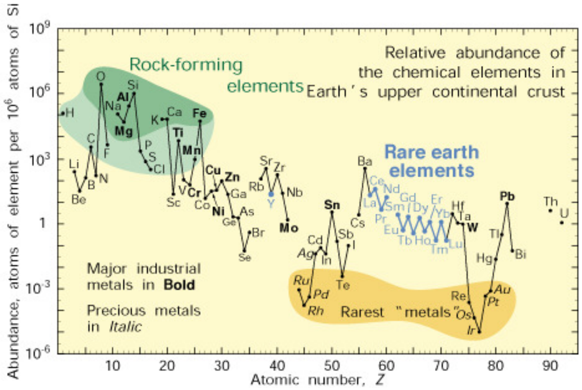

Figure 2: Abundance of each element within the earth's crust. Lithium is somewhat abundant, but other elements such as fluoride and sodium are 10-1,000 times more abundant.[23]

Over the past few decades, several new battery technologies have been suggested, with different options for the charge carrying ion.[90] Most of these, such as Na^+[82][33], Mg^{2+}[99][49] and Ca^{2+}[36][29] batteries, mirror lithium batteries, where a positively charged ion is used to transfer charge, as shown in figure 4. A significant amount of research has been carried out into these types of batteries. However, the use of negatively charged ions to transfer charge, as depicted in figure 5 has been investigated less.[65] Fluoride is one such possibility.[65][61][72] Though the amount of research into fluoride-based batteries has been very limited, it shows promising potential for a number of reasons. Due to the small ionic radius and monovalence of the F^--ion, it has a very high mobility[70] which has interesting implications for its possibility to be used in solid-state batteries. Furthermore, it appears in

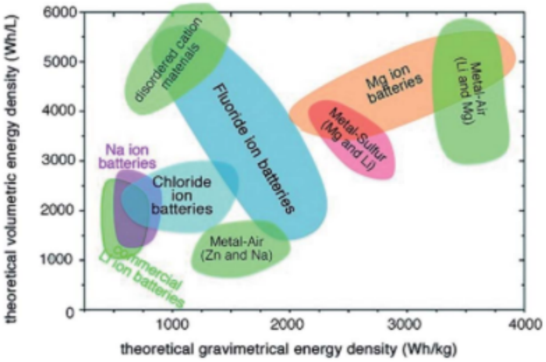

Figure 3: Theoretical energy densities for different battery technologies[65]

compounds in which it has two or three fluoride atoms bound to a single metal atom[72][61], so if these materials could be utilized in a battery, the theoretical energy density of these batteries would be large, as depicted in figure 3. Additionally, fluorine is an abundant element in the earth's crust[23], largely found in the mineral fluorite (CaF_2)[60]. Altogether, this makes fluoride an interesting option to investigate, both as an alternative to lithium-based batteries, as well as a new avenue to approach solid-state batteries.

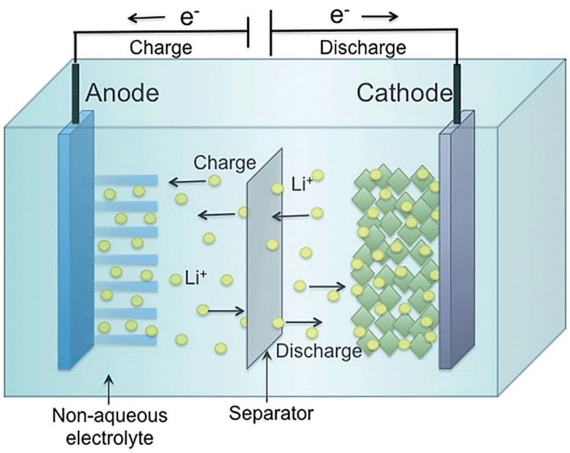

Figure 4: Schematic representation of how a lithium-ion battery works. [25]

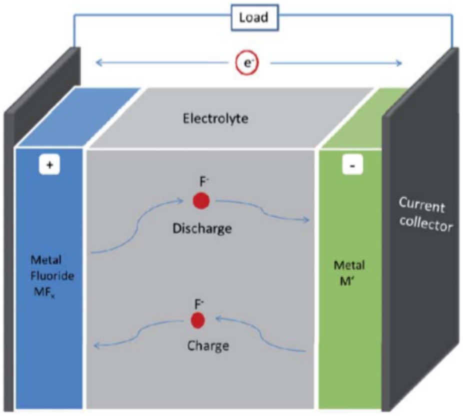

Figure 5: Schematic representation of how a fluoride-ion battery works.[72]

The possibility to make batteries based on the transport of negatively charged F^- ions was first suggested by Baukal in the 1970's[8]. Initial tests were carried out based on the concept, but did not succeed in making working batteries[8][39][38]. It wasn't until 2011 that Reddy and Fichtner released a paper in which they produced a reversible solid-state fluoride-ion battery (FIB)[72]. This battery operated only at 150 °C, and had very poor cyclability. Over the next few years, more interest developed in fluoride-ion batteries, and more research was carried out until in 2018, the group of Mohammad et al. managed to produce a solid-state FIB which operated at room temperature[61].

The ability for fluoride-ion batteries to operate at room temperature was a significant step in the development of the technology, not in the last place because it significantly simplified research that could be carried out on FIB technology. However, the batteries in that paper also suffered from major drawbacks. First of all, the cyclability of the batteries was very poor. Over 75% of the initial capacity was lost after only the third cycle. This is mainly attributed to contact loss between the electrodes and the solid electrolyte, due to the expansion and retraction of the electrode during the charge-discharge cycle. Moreover, the measured initial capacity of these batteries is only 40% of the calculated theoretical capacity, which shows plenty of room for improvement.[61] Some preliminary research has been carried out into selecting promising cathode materials for fluoride-ion batteries. The most promising of these has been found to be BiF_3, which has a high theoretical capacity, and reacts at potentials at which the most widely used solid electrolytes, $BaSnF_4$, $PbSnF_4$ and $La_{1-x}Ba_xF_{3-x}$, are electrochemically stable. The research performed on selecting appropriate anode materials has been less substantial.[65]

This research will look to build onto the work of Mohammad et al. and subsequent publications, and look into potential cathode materials for fluoride-ion batteries. Since research on suitable anode materials has so far been limited, a significant focus of this research will be on symmetrical batteries, in which the cathodic compound will be placed on both sides of the battery, such that while it exists in its oxidized state on the one side, it will exist in its reduced state on the other side. Since BiF_3 has so far been the most promising cathodic material, and $BaSnF_4$ has been a very promising electrolyte material in these types of batteries, a special focus will be placed on these materials in this coming research.

2 Introduction to the theory

This section contains a brief summary of the theory required to understand the experiments performed and the conclusions deduced from them.

2.1 Battery technology

Unless otherwise specified, the material discussed in this chapter is based on the book Advanced Batteries: Material Science Aspects by Robert A. Huggins[32].

Batteries are a form of energy storage in which energy is stored in the form of electrochemical potential. Batteries consist of two electrodes, which contain the materials that undergo the electrochemical reaction, an electrolyte, which seperates the two electrodes and is used to conduct ions, and a metal current collector, which connects both electrodes and is used to conduct electrons. In this section we will discuss the materials that make up a battery, and the performance parameters of a battery.

2.1.1 Battery materials

Batteries consist of two electrodes, a cathode and an anode, which are connected by an electrolyte to facilitate ion transport, and also by a current collector, which facilitates electron transport. In this section we will describe the function of electrodes and electrolyte and discuss what properties are required to make a good electrolyte or electrode.

Electrodes
The electrodes consist of the material that undergoes the electrochemical reaction. During the reaction, one side is oxidized, releasing an electron, which is then transported to the other electrode via the current collector, where the electron reacts with electrode material, reducing it. The side that is oxidized is called the anode, and the side that is reduced is called the cathode. To keep the charge between the two sides balanced, an ion is then transported from one side to the other via the electrolyte. This ion can be either positively charged, in which case it is transported from the anode to the cathode, or negatively charged, in which case it is transported from the cathode to the anode.

The amount of energy that can be stored by the electrode pair is determined by a few factors. The standard reduction potential of each material determines the potential of each reaction. The standard reduction potential is the potential at which a material is reduced relative to the standard hydrogen electrode. The cell potential is given by $V_{cell} = E^C - E^A$ where E^C and E^A are the standard reduction potential of the cathode and anode material respectively. Thus, the higher the standard reduction potential of the cathode, and the lower the standard reduction potential of the anode, the higher the energy yield from the reaction. However, if these values are either too high or too low, the material might undergo undesirable side-reactions, for example by reacting electrochemically with the electrolyte. In that case, the material reacts without the energy being utilized, and the energy of the reaction is lost. Therefore, all other materials in the battery must be electrochemically stable between the standard reduction potential of the cathode and the anode.

The density and valence of the material are also factors that determine the energy density of the cathode. A cathode material that is reduced from M^{3+} to M^0 releases three electrons on reduction and therefore can store three times as much energy as a material that is reduced from M^{3+} to M^{2+}, if everything else is equal.

Bismuth fluoride (BiF_3)
Bismuth trifluoride, BiF_3 is a cathodic material that is has been of interest in both lithium- [31] and fluoride-based batteries [65]. It reduces to metallic bismuth with a standard reduction potential of 0.308 V vs SHE [50]. Due to its trivalence it has a high theoretical energy density [65].

Conversion vs. intercalation based electrodes
Electrode materials can be roughly divided among two categories: conversion and intercalaction based materials.[98][100] Conversion-based materials are materials whose structure is affected when reduc-

tion or oxidation of the material occurs, whereas intercalation-based materials are materials whose structures are unaffected during reduction or oxidation. Generally, conversion-based materials have a higher theoretical capacity, as more of the transport ions (e.g. fluoride ions) are present within the material. However, due to the structural changes within the electrode, conversion-based batteries run into problems of cyclability, where the capacity reduces after a few cycles, due to the change in structure. Intercalation-based materials have a lower theoretical capacity, but generally are more stable over multiple cycles. [65][100]

Electrolyte

The electrolyte is the material that separates the electrodes, and through which ions are transported from one electrode to the other. A good electrolyte has a high ionic conductivity, so that the charge is easily transported through the material. A good electrolyte also has a poor electronic conductivity. Since the electrodes are always connected by the electrolyte, if the electrolyte is a good electron conductor, the reaction can occur even when the current collector isn't connected, and the electrons will not travel via the current collector, so their energy can't be utilized. This is known as self-discharge. [52]

A good electrolyte is also stable between the standard reduction potential of the cathode material and the standard reduction potential of the anode material. If the electrolyte material reacts with the electrode material, the energy released in that reaction can't be utilized and is wasted. This would also affect the structural integrity of the battery. The electrolyte needs to have an electrochemical stability window that encompasses the voltages at which the reactions occur.

Finding electrolytes with high enough ionic conductivity has been one of the main challenges that kept solid-state batteries from performing as well as their liquid-based counterparts. Liquid-based lithium-ion batteries have found electrolytes with conductivities as high as 3.1 mS cm^{-1} [69], whereas solid electrolytes for lithium batteries have electrolytes of only around 0.51 mS cm^{-1} [62]. As fluoride ions are more mobile than lithium ions, electrolytes for fluoride-ion batteries exist with a higher ionic conductivity than that of solid-state lithium batteries. $PbSnF_4$ can have an ionic conductivity of around 1 mS cm^{-1} depending on how it is prepared [78].

Lanthanum fluoride (LaF_3)

For fluoride-ion batteries, one of the first solid electrolytes that was used was lanthanum fluoride. In its pure form, LaF_3 has an ionic conductivity of 10^{-6} S cm^{-1} [72], which is insufficient for an electrolyte material. However, research found that doping the material with Ca^{2+}, Sr^{2+}, Ba^{2+} and Eu^{2+} increases the ionic conductivity of the material significantly. [74][79]. In 2011, Reddy and Fichtner produced a $La_{0.9}Ba_{0.1}F_{2.9}$ sample with an ionic conductivity of $2.8 * 10^{-4}$ S cm^{-1} at 160 °C. They used this material to produce the first rechargeable fluoride ion battery.[72]

Barium tin fluoride ($BaSnF_4$)

Barium tin fluoride is a material that has been used as an electrolyte in room temperature solid state fluoride-ion batteries [61]. The material has a sufficiently wide electrochemical stability window for the use of fluoride-ion batteries. It was found to have an ionic conductivity of 0.7 mS cm^{-1} at room temperature [68], which is deemed sufficient for use in solid-state batteries.

2.1.2 Performance parameters

In this section we will discuss the parameters that determine the performance of a battery. A battery's performance is mainly deduced by the following: its capacity, its voltage, its energy density and its cycle life.

Capacity

The capacity of a battery is the amount of charge that can be stored by that battery. The capacity is dependent on the amount of active material in the battery and the valence of the active material (how many electrons are used in one half-reaction). To be able to compare different batteries, the capacity is usually expressed as specific capacity, where the capacity is divided by the mass of active material. In that case, the molecular mass of the active material also plays a part in the specific capacity. Capacity is usually expressed in either coulombs (C) or ampere hours (Ah), and specific capacity is usually expressed in ampere hours per gram (Ah / g).

Voltage
The voltage of a battery is an expression of the potential of each of the electrons that will be released during discharge. It is determined by the difference of the standard reduction potential of the cathode and the anode. It is expressed in volts (V).

Energy density
The total energy that is stored by a battery is a function of the charge stored (capacity) and the voltage. The energy stored is equal to $E = q * V$. The gravimetric energy density is the amount of energy that is stored per unit of mass. It is often expressed in watt hour per gram (Wh / g). Energy density can also be expressed as volumetric energy density. In this case it is the amount of energy that is stored per unit of volume, and is often expressed in watt hour per centimeter cubed (Wh / cm^3).

Cycle life
The cycle life of a battery is its ability to store energy after having been charged and discharged several times. The capacity decreases through cycling because of several factors: Irreversible electrochemical side-reactions can occur when too high voltages are applied or materials used do not have a sufficiently wide electrochemical stability window; Irreversible chemical reactions can occur if the materials are not chemically stable; Changes in the structure of the electrode can occur that destroy the pathway for ionic or electronic conduction towards the electrode material [92]. Fluoride-ion batteries in particular have suffered from poor capacity retention [72] [65].

2.2 Ionic conductivity

Unless otherwise specified, the material discussed in this chapter is based on the book Semiconductor Physics and Devices - Basic principles by Donald A. Neaman[64].

In order to produce solid-state batteries, materials are required with a sufficient ionic conductivity. The electrolyte needs to have a high ionic conductivity to transport the ions from one electrode to the other. The electrode materials also need to have adequate ionic conductivity to make sure all of the electrode material can undergo reaction, not just the material that is at the electrode-electrolyte surface. This chapter will go into depth on ionic conductivity in solids.

Conductivity mechanisms
In an ideally crystalline structure at a temperature of 0 K, all ions are arranged in a regular periodic fashion, and usually placed in a close-packed form. This means all ions have only enough space available for vibration around their equilibrium. In this situation, ion transport is impossible. In any realistic material and at higher temperatures however, defects in the crystalline structure will be present. These defects allow ionic conductivity to occur. Several different types of defects exist. For ionic conductivity, the most relevant types of defects are the so called *point defects*. These are the defects where the periodic structure deviates from the norm at one specific point in the lattice. The two point defects that are relevant for ionic conductivity are *Schottky defects* and *Frenkel defects*. [44]

A Schottky defect is a point defect where a pair of ions, one negatively charged and one positively charged ion, are missing from the crystal structure altogether. In a Frenkel defect, either a cation or an anion is missing from one point on the lattice, but an ion of that type is present at a different place nearby in the lattice, in between normal lattice points as an *interstitial*. Schottky and Frenkel defects are depicted in figure 6.

Ionic transport occurs mostly through these two types of defect. When a lattice site is vacant due to either a Schottky or a Frenkel defect, neighbouring ions can move to the unoccupied space in the material. This process is called *vacancy migration*. The interstitial ion in a Frenkel defect is also able to move into neighbouring interstitial positions in the lattice, in a process known as *interstitial migration* [44]. A material that contains a more significant amount of such defects has a higher ionic conductivity.

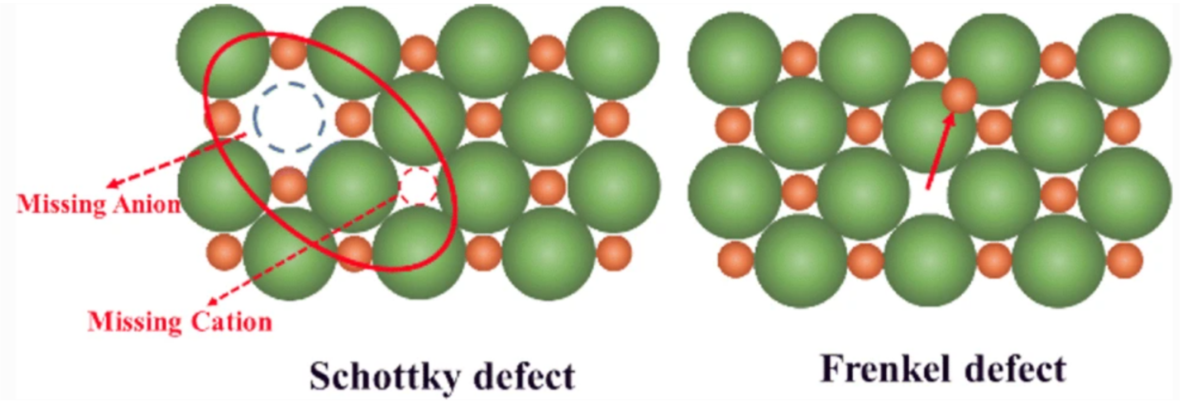

Figure 6: Schottky and Frenkel defects [80]

The amount of vacancies present per unit volume is dependent on quite a few factors, such as the structure, the temperature, presence of impurity ions, the nature of chemical bonding between constituent ions, etc. [44]. On top of that, the ionic conductivity of a material depends on the concentration of charge carriers, the temperature of the material, and the ease with which an ion can jump to another site. The latter factor is related to the mobility of the ion that is to be conducted, which itself depends on the size and charge of the ion [75].

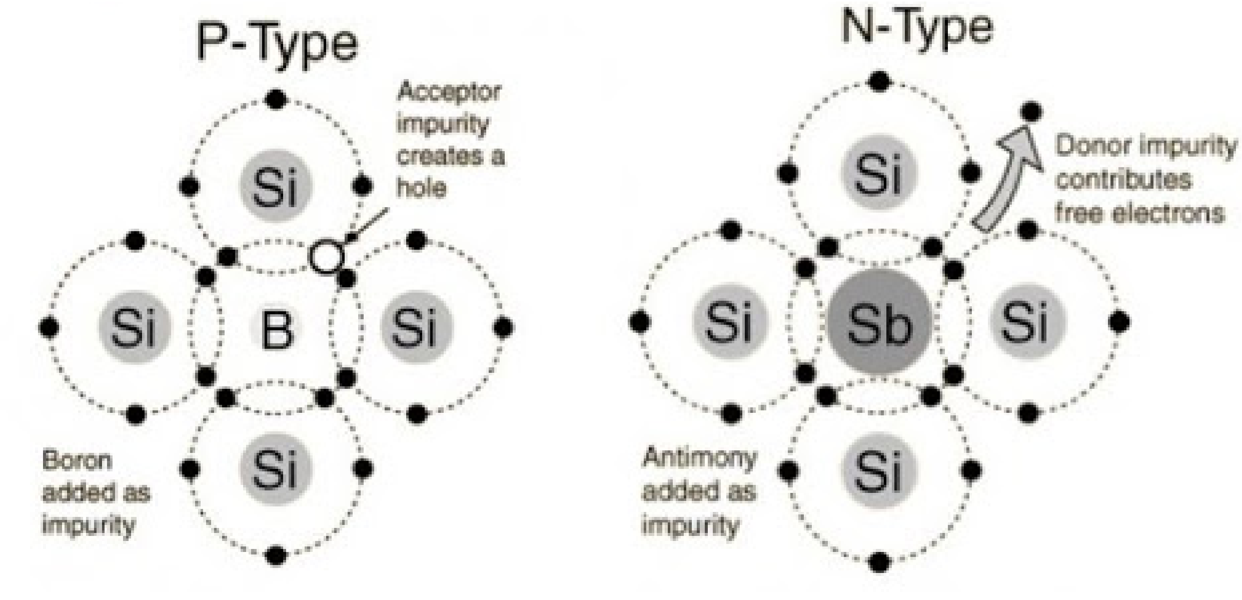

Figure 7: Effect of doping a material with either a lower-valence (left) or a higher-valence (right) material [77]

Besides the intrinsic vacancies that are present in a material, vacancies can also be introduced into a material through doping. Doping is the process of replacing a small number of ions with ions of a material that is similar in ionic radius, so as not to affect the crystalline structure. The dopant ions can have a different valence to the main material. If a dopant cation for example, has fewer anions bound to it due to its lower valence, this introduces a vacancy in the material, similar to that of a Schottky-type defect. If a dopant cation has one more anions bound to it than the main material, due

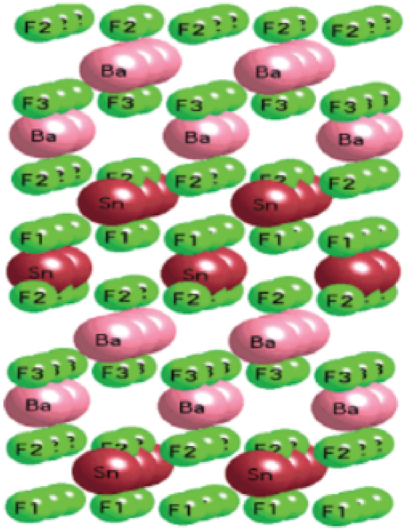

Figure 8: The structure of $BaSnF_4$ [11]

to having a higher valence, for instance, the extra anion takes position in an interstitial point in the lattice, where it can move more freely than when it takes position in a regular point in the lattice. Both effects are illustrated in figure 7. Both introducing lower- and higher-valence dopants can improve the ionic conductivity of a material. [97]

Lanthanum fluoride

In the case of lanthanum fluoride, a material that is used as an electrolyte for fluoride-ion battery applications, doping was used to significantly increase the ionic conductivity of the material. CaF_2, SrF_2, BaF_2 and EuF_2 were all used as dopants.[22][74][79] In this case, the La^{3+}-ions, which are bound to three F^--ions each, are at a few points in the lattice replaced by ions with a lower valence of 2+, and only two F^--ions bound to them. At these points in the lattice, one of the anion positions is vacant, which causes an increase to the ionic conductivity similar to that caused by Schottky defects. Doping in such a way can lead to an increase in ionic conductivity of a factor 100.[72]

Barium tin fluoride

Barium tin fluoride ($BaSnF_4$) is an electrolyte material that has been found to have significant ionic conductivity, of up to 0.7 mS cm^{-1} [68]. It has been used to produce solid state fluoride-ion batteries at room temperature [61]. In 2002, Chaudhuri et al. used nuclear magnetic resonance (NMR) techniques to deduce the transport mechanism for fluoride ions in barium tin fluoride [11].

Barium tin fluoride has a structure of -Ba-Ba-Sn-Sn-Ba-Ba-Sn-Sn- where double layers of BaF_2 are alternated with double layers of SnF_2 as depicted in figure 8. In this figure, three different types of fluoride-ions are noted. Fluoride ions labeled F1 are the fluoride ions that are in between two tin layers. The ones labeled F2 are the fluoride ions that are in between a tin and a barium layer. The fluoride ions labeled F3 are between two barium layers. From the NMR research, Chaudhuri et al. found that the F1 and F2 fluoride ions are a large factor in the ionic conductivity, but that the F3 fluoride ions, which are between two barium layers, do not significantly contribute to the ionic conductivity [11].

2.3 Techniques utilized

This section will contain a brief summary of the techniques used in the experimental part below. For the analysis of the structure and the characterization of the materials making up our samples, X-ray diffraction was used, which is described in subsection 2.3.1. To test the ionic conductivity of materials, impedance spectroscopy was used, which is described in section 2.3.2. To test the batteries that were produced by combining these materials, galvanostatic cycling was used, which is described in section 2.3.3.

2.3.1 X-Ray diffraction

X-ray diffraction is a non-destructive method that can be utilized to characterize materials and find information on the size, shape and orientation of its crystallic structures [2]. The theory behind X-ray diffraction will be explained, and the basic structure of several of the materials analyzed in these experiments will be shown.

Crystalline structures

Each structure is either a crystalline, polycrystalline or amorphous structure. A crystalline structure is one in which the atoms have arranged themselves in a regular, repeated pattern. In an amorphous structure, the atoms arranged themselves in an irregular pattern. A polycrystalline structure consists of several small crystalline phases which are oriented differently from each other.

A crystallic structure can thought of as made up of *unit cells*. A unit cell is the smallest possible structure that can be repeated in all three dimensions to form the complete crystalline structure. Auguste Bravais described *Bravais lattices* to characterize these unit cells. He found 14 different structures which together described all possible arrangements of points in a lattice space, depending on the distances and angles between the atoms. These are shown in figure 9.

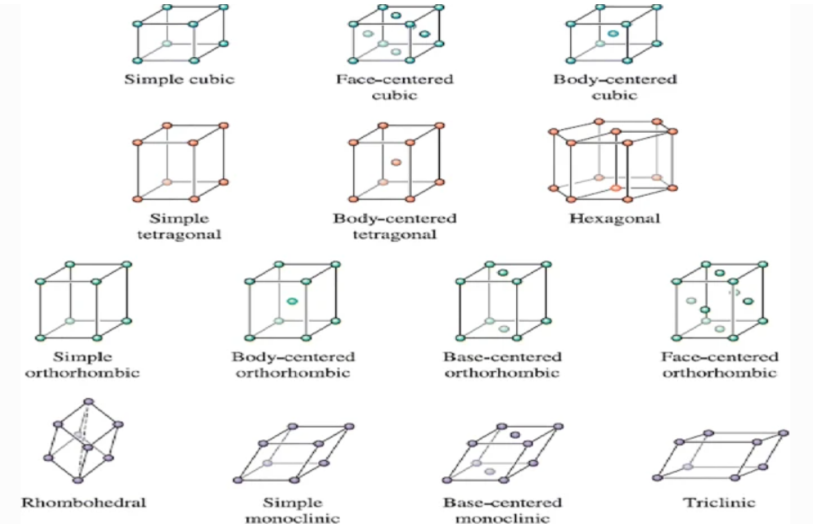

Figure 9: All of the 14 Bravais lattices [3]

Any plane within the crystal structure can be described using Miller indices. To derive the Miller indices, an xyz-axis system is set up along the angles of the unit cell. The Miller indices h, k and l are then the reciprocals of the intercept of the plane against the x, y and z-axis respectively. If the plane is parallel to one of the axes, the corresponding intercept is taken as infinite, so the reciprocal is taken as 0. For example, (100) are the Miller indices of a plane parallel to both the y- and z-axis. Figure 10 shows several planes described by their Miller indices.

Crystalline structure of materials used

The crystalline structure of several of the materials used in these experiments are shown in table 1.

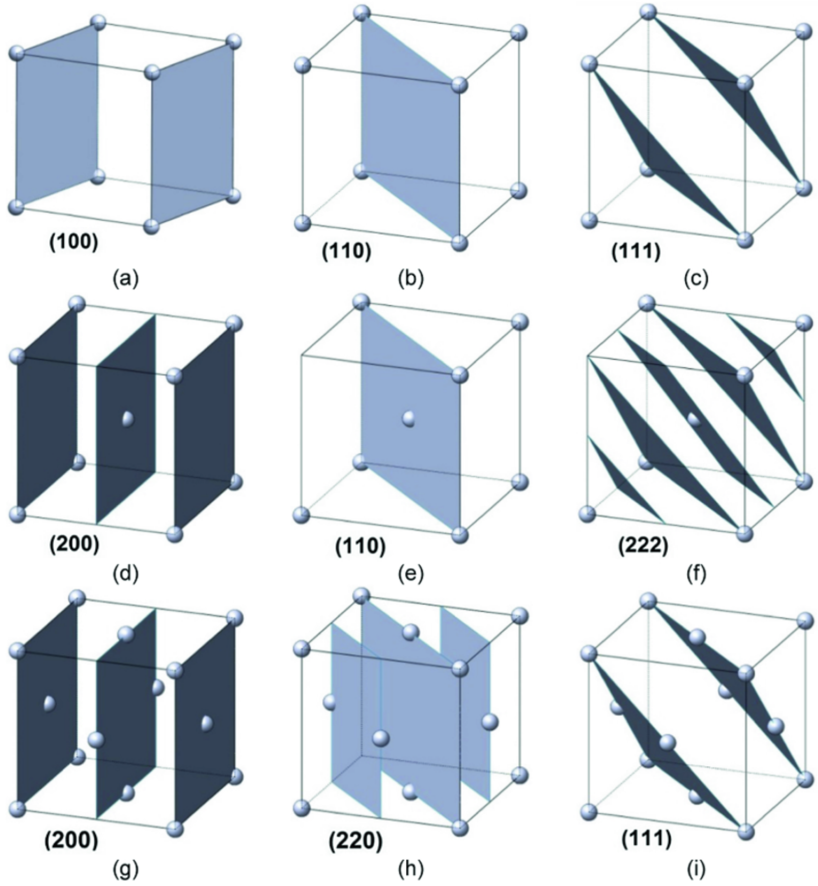

Figure 10: Several planes described by their Miller indices. [87]

Material	Symmetry	a (Å)	b (Å)	c (Å)	α (deg)	β (deg)	γ (deg)	Space group	Ref.
c-$BaSnF_4$	cubic	6.1990	6.1990	6.1990	90	90	90	Fm$\bar{3}$m	[1]
t-$BaSnF_4$	tetragonal	4.3450	4.3450	11.2280	90	90	90	P4/nmm	[1]
o-BiF_3	orthorhombic	5.010	6.547	7.104	90	90	90	Pnma	[57]
h-BiF_3	hexagonal	4.124	4.124	7.028	90	90	120	P6_3/mmc	[40]
c-BiF_3	cubic	4.076	4.076	4.076	60	60	60	Fm$\bar{3}$m	[58]
Bi_2O_3	monoclinic	5.8486	8.1661	7.5097	90	113	90	P2_1/c	[53]
BiOF	tetragonal	3.7469	3.7469	6.2260	90	90	90	P4/nmm	[4]
$Bi_7O_5F_{11}$	monoclinic	13.5094	5.5223	9.1793	90	96.158	90	C2	[46]
Bi_2OF_4	cubic	5.8195	5.8195	5.8195	90	90	90	Fm$\bar{3}$m	[47]
$BiO_{0.55}F_{1.9}$	cubic	5.8195	5.8195	5.8195	90	90	90	Fm$\bar{3}$m	[47]
$BiO_{0.09}F_{2.82}$	hexagonal	4.0980	4.0980	7.2770	90	90	120	P6_3/mmc	[5]

Table 1: Crystalline structures of several of the materials used in the experiments below

Diffraction

Diffraction is a phenomenon that occurs when waves encounter an obstacle or opening. In this, the waves bend around the obstacle. If waves pass through a slit with a width that is in the same order of magnitude as the wavelength of the waves, the waves will then spread out past the slit due to them bending around the walls of the obstacle. [63] This is shown in figure 11. When multiple of these slits are located close to each other, constructive and destructive interference will take place and a unique pattern of the waves will be created, as shown in figure 12

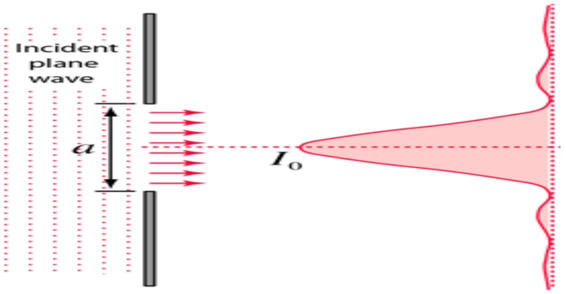

Figure 11: Waves passing through a single slit [63]

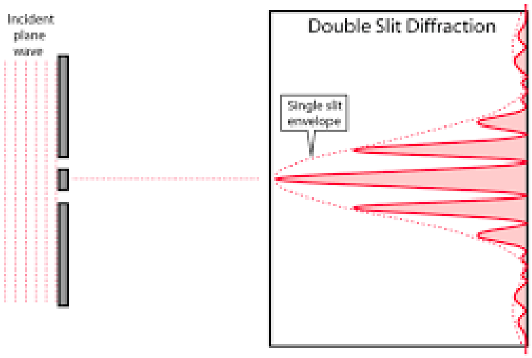

Figure 12: Waves passing through two slits [63]

Bragg's law
During X-ray diffraction, X-ray's are incident on a crystalline material. These X-ray's have a wavelength of the same order of magnitude as the distance between the atoms in the crystalline material. Therefore, the spaces between these atoms cause the X-rays to undergo diffraction. Because of the large number of atoms in the material, this can be considered a diffraction with infinite slits. The diffracted X-rays will give a pattern whose intensity depends on the distance between the atoms and the angle at which X-rays are incident on the material. The relationship is given by Bragg's law: $n\lambda = 2dsin(\theta)$, with n the diffraction order, λ the wavelength, d the distance between the atoms of the material, and θ the angle of the X-rays incident on the material, as shown in figure 13 [2]. The distance between the atoms, d, differs per material, but also depends on the miller indices of the plane in question.

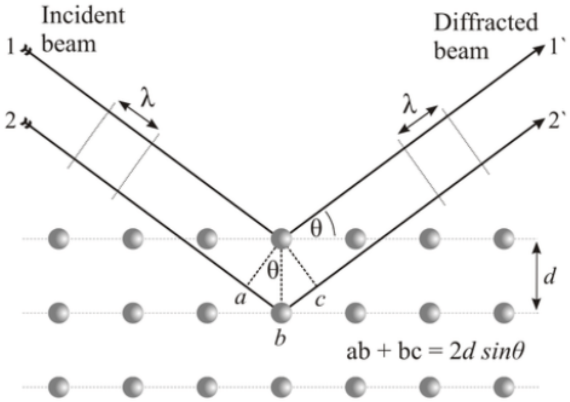

Figure 13: Bragg diffraction [19]

Every crystalline solid material has a unique X-ray diffraction pattern. These patterns can be used to identify materials present in a sample, as well as their crystalline size, residual stress and strain, lattice parameters, dislocation density and many other characteristics.

2.3.2 Electrochemical Impedance spectroscopy

Electrochemical Impedance Spectroscopy (EIS) is a non-destructive method that can be used to characterize the electrochemical properties of a material.[66] It usually involves applying a small sinusoïdal voltage to the material and measuring the response current. From that, the impedance can be deduced.

Impedance

Impedance is the measure of opposition to electrical flow. For Direct Current (DC) systems, impedance is equal to resistance, which is governed by Ohm's law: $V = IR$, or $V/I = R = Z$. In an Alternating Current (AC) system, the impedance is different from the resistance when the voltage and current of the system are out of phase. In this case, there is a phase shift θ, which means that the impedance is equal to $Z = \frac{E(t)}{I(t)} = \frac{|E|sin(\omega t)}{|I|sin(\omega t+\theta)}$ where ω is the angular frequency. [71]

Measuring impedance

Impedance is usually measured by applying a short sinusoïdal voltage to the system and measuring the response current. [71] This measurement can be carried out at different frequencies. By measuring at different frequencies, different processes can be analyzed in isolation. At high frequencies, high speed processes such as ion migration will respond, whereas at low frequencies, slower processes such as diffusion dominate.[85] Impedance results are usually plotted in Bode or Nyquist plots. Bode plots plot either the magnitude or the phase of the impedance against the applied frequency. Nyquist plots are parametric plots that plot the negative imaginary part of the impedance against the real part of the impedance. A typical plot for each is shown in figure 14.

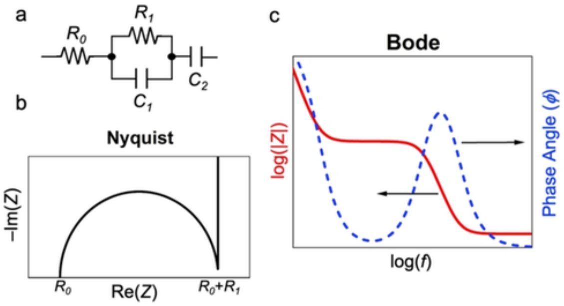

Figure 14: Typical Bode and Nyquist plots [85]

Equivalent circuits

To analyze the results from the impedance measurement, the concept of equivalent circuits is used. In an equivalent circuit, the system that was measured is modeled using circuit elements. A common Nyquist plot, such as the one shown in figure 14, mainly consists of a semicircle. This can be modelled in an equivalent circuit by a resistance (representing surfance resistance) in series with a resistance and a capacitance in parallel (representing bulk resistance and capacitance respectively).[45] Usually, the capacitance of the system behaves non-ideally, and to compensate for that, the capacitor is replaced by a constant phase element (CPE). [85]

Deducing ionic conductivity

To use this equivalent circuit to deduce the ionic conductivity, we are interested in the bulk resistance of the material. This is equal to the real impedance at the point where the semicircle intersects the real axis, at the right side (lower frequency side) of the semicircle, as shown in figure 15. The bulk resistance can then be used to deduce the ionic conductivity using the formula: $R = l/(A\sigma)$ or $\sigma = l/(AR)$, where R is the bulk resistance, l is the length of the material (the thickness of the pellet), and A is the area of the material.

Relationship conductivity and pressure

It has been found that an increase in pressure can increase the ionic conductivity of a solid material.[20] As shown schematically in figure 16, at low pressures, the particle-particle contacts are limited. This has two consequences: a smaller effective area (A_{ionic}), and a higher tortuosity (τ), leading to an increased distance that ions have to travel between electrodes [20]. At high pressures, a minimum tortuosity and a maximum effective area is reached, at what is called the critical stack pressure[88]. At higher pressures, no significant increase in ionic conductivity is measured. In fact, a slight decrease in ionic conductivity is measured, due to creep caused by stress on the material [43][56].

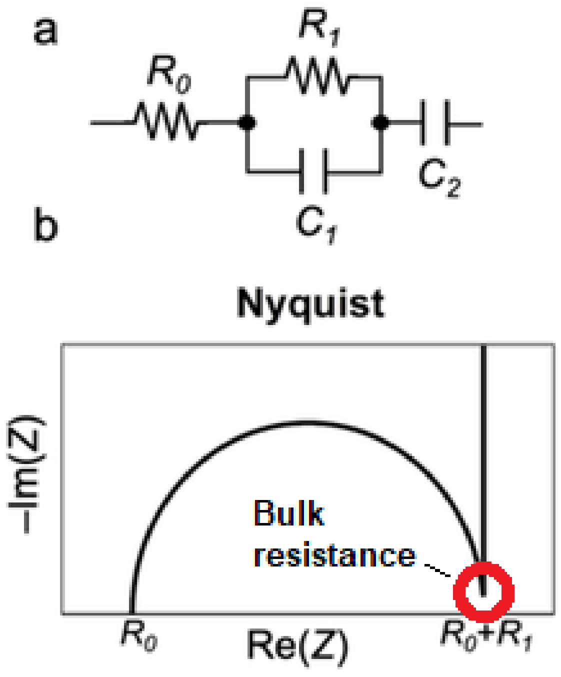

Figure 15: Value of the bulk resistance in a Nyquist plot [85]

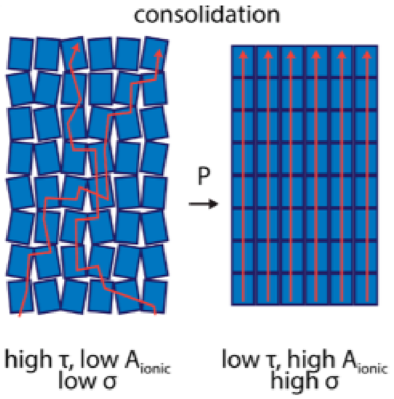

Figure 16: Effect of pressure on the ionic conductivity of materials [20]

Some typical graphs for the ionic conductivity dependence on the applied pressure are shown in figure 17 and 18. Figure 17 shows the ionic conductivity dependence on pressure for Li_6PS_5Cl, an electrolyte material used in solid-state lithium batteries [89], and figure 18 shows the ionic conductivity dependence on pressure for $Li_7P_3S_{11}$, another electrolyte material used in solid-state lithium batteries. [96]

Both these materials show a similar pattern. At low pressures, a small increase in pressure drastically increases the ionic conductivity of the material. At higher pressures, the increase in pressure levels out and the graph becomes flatter. It should be noted that these patterns occur over a span of different pressures. The pressures at which this maximum ionic conductivity is approached differs per material.

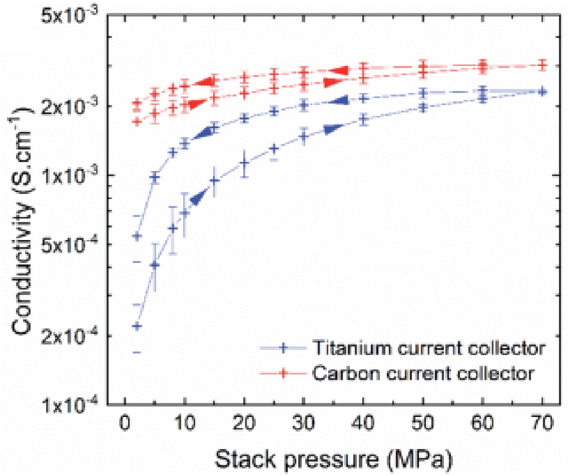

Figure 17: Ionic conductivity dependence on applied pressure for electrolyte material Li_6PS_5Cl with two different current collectors. The pressure was initially increased, and then when the maximum pressure was reached, was decreased again, with the impedance being measured during each. The arrows on the graph show whether the pressure was increasing or decreasing. [18]

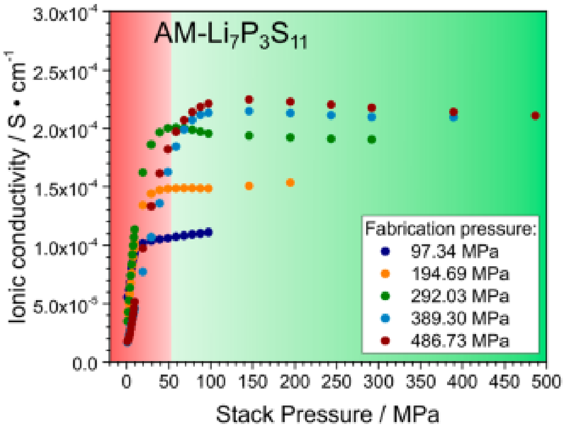

Figure 18: Ionic conductivity dependence on applied pressure for electrolyte material $Li_7P_3S_{11}$ with an amorphous structure. The applied pressure dependence was measured for different fabrication pressures, i.e. different pressures were applied to press the material into a pallet before starting measuring the ionic conductivity effect of increasing the applied pressure from 0 to 500 MPa. [14]

2.3.3 Galvanostatic cycling

Galvanostatic cycling is the most widely used method to analyze battery performance [94]. It involves applying a constant current to the battery to drive an electrochemical reaction, followed by a reverse current to drive the reverse reaction [30]. The potential response is then recorded.

Open-Circuit Voltage

The open-circuit voltage of a cell is the difference in potential between the two sides of the battery when no current can flow between either side of the battery. It gives an indication to the strength of the driving force in spontaneous discharge in the battery. A high open-circuit voltage in a battery gives a high theoretical energy density, as the energy is calculated by $E = q * V$ where E is the energy, q the charge, and V the voltage. The open-circuit voltage is defined by the difference in the standard reduction potential of the half-reactions in each of the electrodes. The voltage of a cell is governed by the Nernst equation: $E_{cell} = E^{\circ}_{cell} * \frac{RT}{zF} ln(\frac{a_{Red}}{a_{Ox}})$ where E°_{cell} is the standard cell potential, the difference between the standard reduction potential of the cathode and the standard oxidation potential of the anode, R is the gas constant, T is the temperature, z is the number of electrons transferred per half reaction, F is the Faraday constant, and a_{Ox} and a_{Red} are the activity of the reductant and the oxidant, and can usually be approximated by the concentration of each.

Symmetric batteries can be made in which the half reaction in the cathode is the reverse reaction of the half reaction in the anode. Here, the open-circuit voltage of the battery is equal to 0V. These symmetric batteries cannot be used to effectively store energy as the open-circuit voltage is too low, but they are a useful tool to research electrode materials, as having the same half-reaction occur on both sides reduces the number of variables affecting the battery performance.

Actual cell potential

When a current is applied to a cell, the potential becomes lower than the open circuit voltage. The actual potential of a cell is lower than the theoretical potential, which is mainly due to three sources of irreversible losses: activation polarisation, concentration polarisation and Ohmic polarisation [59]. This is shown in figure 19. The actual cell potential is given by $V_{cell} = E^C - E^A - \eta_A - \eta_C - iR_{cell}$, where E^C and E^A are the cathode and anode potential respectively, η_A is the activation polarisation, η_C is the concentration polarisation, and R_{cell} is the resistance of the cell.

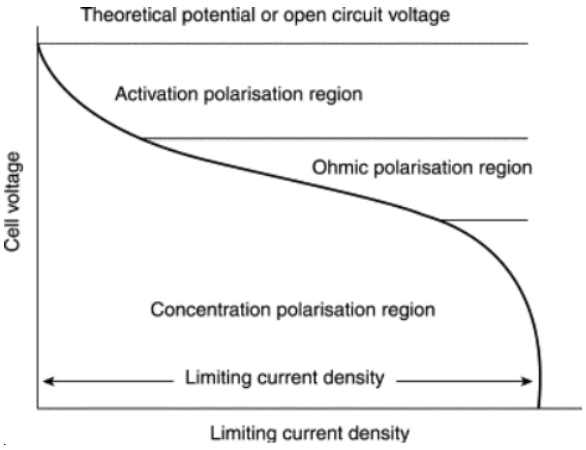

Figure 19: Effects of different irreversible losses on cell potential [59]

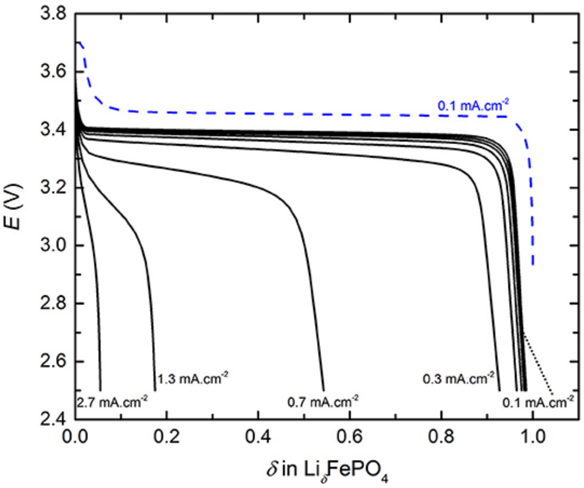

Figure 20: Example of the typical effect of current density on the voltage behaviour of a cell during galvanostatic cycling [17]

The overpotential is the difference between the theoretical voltage at which a reaction would have occured and the voltage at which the reaction is observed. This is directly related to the voltage efficiency of the reaction.

Current density

The applied current to the cell is usually expressed as current density, so it can be compared to batteries of different diameter. The current applied to the battery affects its characteristics. Figure 20 shows an example of the typical effect of different current densities on the voltage results of a cell. In this example, the behaviour of the current density on the voltage during discharge is shown for a Li$_\delta$FePO$_4$ material. This material is commonly used in lithium-ion batteries as a cathode material [17]. Unlike for example BiF$_3$, it is an intercalaction-based material, so the behaviour under different current densities may differ from that of conversion-based materials.[65] [83]

From the graph, we find that at low current densities, once the voltage of the cell is lowered to the voltage where the reaction occurs, the voltage stops decreasing. This is the moment when the reaction occurs. The voltage stops decreasing because the current that is applied to the cell is “consumed” by the reaction. Once all active material (that can be reached by the current) has reacted, the voltage will start decreasing again. At too high current densities however, the limiting factor is not the current, but the diffusion rate of the ions that are to be transported from the cathode to the anode or vice versa (dependent on the charge of the ion) [21]. At these current densities, no voltage plateau is visible in the graph. Instead the voltage keeps decreasing. This is the case for the current density of 2.7 mA cm^{-2} in the example figure 20.

The current density at which ionic diffusion rates start becoming dominant is called the critical current density [21]. The value of this depends on the diffusion rate, which in turn depends, among other things, on the resistance of the cell [10].

Current fluoride-ion battery experiments generally use a low current density, ranging from 4.5μA [27] to 40μA [16]. These low current densities lead to a low power output for the batteries and are a characteristic that needs to be improved. The low current densities are necessitated in part by the low ionic conductivities of the electrode materials that are used for the batteries.

The current density also determines the C-rate of a battery. The C-rate describes the rate at which a battery is (dis)charged. It is equal to the current applied to the battery divided by the current required to deliver the nominal capacity of the battery in the timespan of one hour. [7]

2.4 Fluoride-ion batteries

In the following section we will discuss the literature that has previously been published on the development of solid-state Fluoride-ion batteries.

First fluoride-ion batteries

Batteries based on the shuttle of fluoride ions were first suggested by Baukal in the 1970's [8][65]. Initial experiments were performed based on the concept, but no batteries were produced [38][39].

In 2011, the group of Anji Reddy and Fichtner first produced working fluoride-ion batteries.[72] At the time, no liquid material had been found that could function as an electrolyte. Several solid materials were known to sufficiently conduct fluoride ions at elevated temperatures. Lanthanum fluoride (LaF_3) specifically was deemed of interest. As a pure material, it had an ionic conductivity of $1 * 10^{-6} Scm^{-1}$ at room temperature [72]. Doping with either Ca^{2+}, Sr^{2+}, Ba^{2+} or Eu^{2+} was known to drastically improve the ionic conductivity [22][81][79]. Anji Reddy and Fichtner produced $La_{1-x}Ba_xF_{3-x}$ ($0 \leq x \leq 0.15$), and found that a maximum ionic conductivity of $2.8 * 10^{-4} Scm^{-1}$ was reached for $La_{0.9}Ba_{0.1}F_{2.9}$ at 160 °C. This is the material they used as an electrolyte to produce fluoride-ion batteries.

As a cathode, Anji Reddy and Fichtner tested CuF_2, BiF_3, SnF_2 and $KBiF_4$. SnF_2 and $KBiF_4$ had high ionic conductivity, but CuF_2 and BiF_3 did not, so the latter two were combined with electrolyte material to produce a cathodic compound. All four materials also had carbon added to the cathodic compound to improve electronic conductivity. Cerium metal was chosen as an anode material.

These combinations of materials produced fluoride-ion batteries with discharge capacities of 126 mAh/g to 322 mAh/g. The cycling behaviour of the battery with BiF_3 as a cathode was analyzed in-depth. They found that the discharge capacity decreases sharply during the first few cycles and then gradually decreases until it reached about 50 mAh/g after 38 cycles.

Symmetric Bi/BiF_3 battery

In 2016, Grenier and his team published a paper that involved a symmetric Bi/BiF_3 battery, with a $La_{0.95}Ba_{0.05}F_{2.95}$ electrolyte [27]. The battery was operated at 150 °C and was covered in an epoxy resin to prevent air from reacting with the battery. BiF_3 is a material that is sensitive to oxygen. When it comes in contact with air, it can react to form oxides.[9] The formation of these oxides are hypothesized to have a detrimental effect on the ionic conductivity of the electrode. Therefore, the material is usually handled under inert atmospheres. For performing galvanostatic cycling on these batteries, inert atmospheres are generally infeasible however. Thus, Grenier devised a method to cover the battery in an epoxy resin, which should prevent the battery materials from coming into contact with oxygen. Using this epoxy resin, the authors of the paper found a much higher discharge capacity retention, with discharge capacities of around 180 mAh/g for each of the first three charge-discharge cycles.

Barium tin fluoride

In 2014, Preishuber-Pflügl and his team published a paper discussing a new method of producing $BaSnF_4$ [68]. Previously, tetragonal $BaSnF_4$ was known as a material with an outstanding ionic conductivity at room temperature. The ionic conductivity did appear to be very dependent on the method used to produce the material.

Preishuber-Pflügl and his team produced $BaSnF_4$ by using high-energy ball-milling, ball-milling stochiometric amounts of BaF_2 and SnF_2. The resulting material had a large amount of defects, which led to a high ionic conductivity. They found it to have an ionic conductivity of $7 * 10^{-4} Scm^{-1}$. Due to its high ionic conductivity as room temperature, this material became of interest as a solid electrolyte in Fluoride-ion batteries.

In 2020, the group of Wang released a paper in which they doped $BaSnF_4$ with NdF_3 to produce an electrolyte with an even higher ionic conductivity [51]. Adding a trivalent dopant to the electrolyte material increases the concentration of interstitials, which have a higher ionic conductivity than regularly placed ions.[64] Thus replacing some barium ions with neodymium ions increases the ionic conductivity of the material. They found that for $Ba_{1-x}Nd_xSnF_{4+x}$ the highest ionic conductivity was achieved at x = 0.02.

Room temperature FIB

In 2018, Mohammad and his team published a paper in which they report fluoride-ion batteries that are operated at room temperature [61]. The battery consisted of BiF_3 as a cathode, t-$BaSnF_4$ as an electrolyte and either Zn or Sn metal as an anode. The battery with metallic tin as an anode had a discharge capacity of 120 mAh/g, which quickly decayed to around 5 mAh/g after 10 cycles, but the battery with metallic zinc as an anode had a discharge capacity of 55 mAh/g after the first cycle, which increased to around 60 mAh/g after 9 cycles. These results are shown in figure 21.

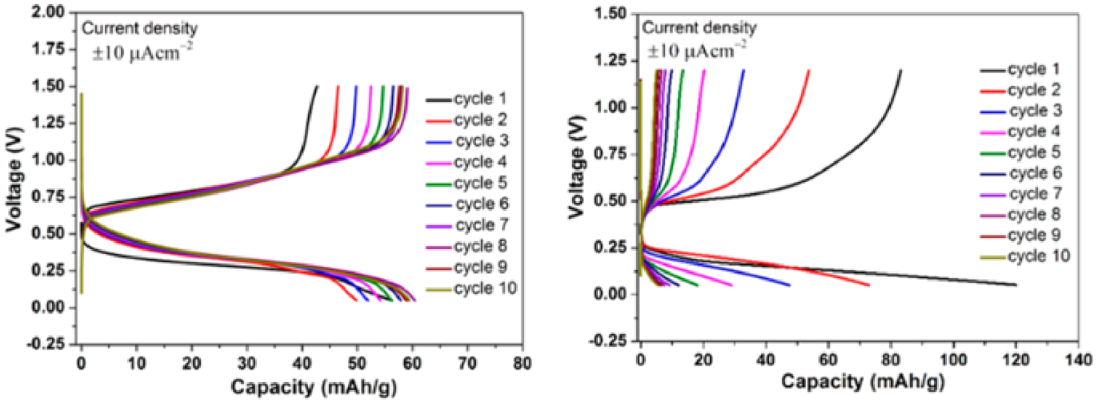

Figure 21: Results from the room-temperature FIB measurements. The graph on the left shows the battery with a Sn anode, and the graph on the right shows the battery with a Zn anode.[61]

This established the possibility of room-temperature fluoride-ion batteries. The $BiF_3|BaSnF_4|Sn$ batteries at room-temperature had a capacity of 40% of the theoretically calculated capacity during the first cycle, and it significantly reduced during subsequent cycles. The $BiF_3|BaSnF_4|Zn$ batteries had a capacity of 18% of the theoretically calculated capacity furing the first cycle, though it reduced less substantially on subsequent cycles.

One possible explanation that caused the capacities to be significantly lower than the theoretically calculated values was formation of oxide. BiF_3 is sensitive to oxygen[9], and as Grenier showed, shielding the battery from exposure to air improves the battery characteristics.[27]

Some of the drawbacks for these batteries might be improved through adjusting the cathode material. BiF_3 has a low ionic and electronic conductivity, and thus a composite cathode is used, consisting of BiF_3, electrolyte for ionic conductivity, and carbon for electronic conductivity. When the battery charges and discharges, the cathode material expands and shrinks significantly in size. This is hypothesized to erode the BiF_3-electrolyte contact, and thus preventing ions from being transported to or from the cathodic material, making the reaction impossible. Another challenge in current fluoride-ion battery technology is the charge and discharge rate. Current fluoride-ion battery experiments use very low current densities, of 4.5 μA cm^{-2}[51] to 40 μA $cm011^{-2}$[16]. These low current densities are necessitated by the low rate of transport of fluoride ions from cathode to anode, which is so low in part due to the relatively low ionic conductivity of the electrode materials. Improving the ionic conductivity of the electrode materials would be an important step in improving the current densities.

BiF_3 doping

One of the main roads to improving fluoride-ion batteries was hypothesized to be improving the ionic conductivity of BiF_3. BiF_3 is a promising cathode material due to its high theoretical capacity and its appropriate standard reduction potential, but it is a poor fluoride-ion conductor, which limits its suitability as a cathode material [65]. This issue was previously tackled by mixing BiF_3 with electrolyte material to form a cathodic compound electrode [72] [61] [27], but this decreases the theoretical capacity of the cathode. A new topic of interest is the doping of BiF_3 with one of several possible materials, which can introduce vacancies in the material, thereby improving fluoride-ion conduction.

From 2017-2021, the group of Ogumi published a series of papers where they, among other things, analyzed the effect of doping BiF_3 with BaF_2 to stabilize different BiF_3 polymorphs [41] [93] [42] [76]. They produced batteries that had $Bi_{1-x}Ba_xF_{3-x}$ (x = 0, 0.2, 0.4) as a cathode, which stabilized an orthorhombic, hexagonal and cubic phase respectively. As an electrolyte, a liquid organic solvent with CsF dissolved in it was used, and as an anode, 2, 4, 6-tris(4-fluorophenyl)boroxine was used. The cathode with x = 0, which had an orhorhombic structure, had discharge capacities of 175, 108 and 53 mAh/g in the first three cycles, while the hexagonal cathode with x = 0.2 had values of 211, 140 and 98 mAh/g for the discharge capacity in those cycles, and the cathode with a cubic structure, with x = 0.4, had discharge capacities of 80, 67 and 58 mAh/g for the three initial cycles. Thus it was deduced that capacity retention was the highest for the cubic structure, which was stabilized by a 40% BaF_2 dopant concentration. Capacity was the highest for the hexagonal structure, which was stabilized by a 20% BaF_2 concentration.

One potential problem with using barium-doped bismuth fluoride, is that when in reduced state, bismuth may seperate from barium. Barium does not form alloys well with bismuth.[6] One material that does form alloys well with bismuth and that also has an appropriate standard reduction potential, is tin.[6] Tin has an oxidation state of 2+, which is one fewer than that of bismuth, which would suggest that doping bismuth fluoride with tin fluoride would improve ionic conductivity due to the addition of extra vacancies.

In 2015, the group of Pei published a paper in which first principle studies were carried out on doping BiF_3 with SnF_2 for the purpose of using this material as a cathode in lithium-ion batteries. It found that the ionic conductivity of BiF_3 can effectively be improved by doping with tin flyirude [95]. No experimental work has currently been published where tin-doped bismuth is used as a cathode material in fluoride-ion batteries.

Next steps in Fluoride-ion batteries

Room-temperature fluoride-ion batteries have been produced by Mohammad et al.[61]. Despite fluoride-ion batteries having a high theoretical capacity, the experiment failed to reach these high capacities, as well as showing poor capacity retention through multiple cycles. Besides that, the batteries operate only under low current densities. An important question in this field is how these values can be improved. The presence of oxides is hypothesized to be one of the causes of the low capacity values. This effect needs to be more thoroughly examined. It is also hypothesized that improving the ionic conductivity of the cathodic material through doping, for example with tin fluoride, can improve the low current densities. The effect of oxides in BiF_3 and the effect of doping BiF_3 with SnF_2 are questions that will be looked into in the following sections.

3 Experimental

The experimental work consisted of several different types of measurements, which were repeated several times with different materials and different circumstances. In the following section, a general description of all the experimental procedures will be given. The details of each experiment, including the amounts of material used will be provided later, in section 4.

3.1 Copper tubes

Sealed copper tubes were used to transfer materials from the glovebox to a furnace without exposing the materials to oxygen or humidity. Any tubes used in the experiments were cleaned by first annealing them in a Nabertherm Compact Tube Furnace for 1 h at 300 °C under a flow of N_2-gas (Linde), with a 1 h ramp up time for the heat. Then, the tubes were removed from the tube oven and placed in 1 M HCl (made from HCl (Sigma Aldrich >37%) and demiwater (Emergo)) for 10 minutes, after which they were neutralized in 0.1 M NaOH (made from NaOH (Sigma Aldrich, >85%) and demiwater (Emergo)). Then they were scrubbed with a metal brush, placed in more 1 M HCl, and sonicated in a Bandelin Sonorex Digital 10p ultrasonic bath for 15 minutes. Afterwards they were neutralized in more 0.1 M NaOH. The copper tubes were placed under an inert atmosphere of 1 atm argon (Linde). Under this inert atmosphere, the tubes were filled with the material that was to be annealed, and sealed by flattening and folding the tubes using a Syrio Dental P400 hydraulic press.

3.2 Synthesis of $BaSnF_4$

Tetragonal barium tin fluoride was used as an electrolyte for producing fluoride-ion batteries, and was researched seperately. It was produced by mixing barium fluoride and tin fluoride in stochiometric amounts under inert atmosphere. It then either underwent high-energy ball-milling to produce cubic barium tin fluoride, which was then thermally annealed to produce tetragonal barium tin fluoride, or it was directly annealed to tetragonal barium tin fluoride.

To mix the barium tin fluoride, stochiometric amounts of VWR 99% BaF_2 and Acros Organics 99% SnF_2 were weighed on a Sartorius BP301S scale in a MBRAUN UNIlab glovebox filled with 1 atm argon (Linde). The powders were briefly mixed by hand in a pestle and mortar. If the material was to undergo high-energy ball-milling, the powder was then placed in a ball-milling jar which was filled with ZrO_2 balls with a diameter of 5 mm, with a weight ratio powder to balls of 1:30. The number of ball-milling cycles, the number of rotations per minute, the length of each cycle, and the length of the rests between cycles differed per instance, and will be listed for each specific experiment in section 4.

Materials that were to be annealed were placed inside a copper tube in the glovebox, which was cleaned and sealed as detailed in section 3.1. The sealed tube was then removed from the glovebox and placed in a Nabertherm Program Controller S27 furnace. The temperature and time for the annealing is listed for each specific experiment in section 4.

3.3 Synthesis of $BiO_{1.5x}F_{3-3x}$

To produce bismuth oxyfluorides, BiF_3 (FluoroChem, 99%) and Bi_2O_3 (Thermo Fischer, 99.9%) were mixed by hand in a pestle and mortar in a MBRAUN UNIlab glovebox filled with 1 atm argon (Linde). Then the powder was pressed into a pellet with a diameter of 6 mm, by applying roughly 130 MPa for 5 minutes using a Syrio Dental P400 hydraulic press. Then, the pellet was placed in a copper tube which was cleaned and sealed according to the steps in section 3.1, and removed from the glovebox. It was placed in a Nabertherm Program Controller S27 furnace. The time and temperature was different for each measurement and will be listed for the specific experiments in section 4.

3.4 Synthesis of $Bi_{1-x}Sn_xF_{3-x}$

Tin-doped bismuth fluoride was prepared by, in a MBRAUN UNIlab glovebox filled with 1 atm argon (Linde), weighing on a Sartorius BP301S scale, BiF_3 (either FluoroChem, 99% or ApolloScientific, 99.99%) and SnF_2 (Aldrich, 99%), and mixing them by hand in a pestle and mortar. Then, pellets with a diameter of 6 mm were pressed out of the material by applying ca. 130 MPa for 5 minutes using a Syrio Dental P400 hydraulic press. The pellet was placed in a copper tube that was cleaned and sealed using the method described in section 3.1, and was removed from the glovebox. The tube was then placed inside a Nabertherm Program Controller S27 furnace, where it was thermally annealed. The temperature and time of the annealing step differed for each measurement and is listed seperately in section 4.

3.5 XRD measurements

To perform XRD measurements, roughly 200 mg of a sample was weighed on a Sartorius BP301S scale. In some cases this will have been performed under an inert atmosphere. In that case this will be done in a MBRAUN UNIlab glovebox filled with 1 atm argon (Linde). The powder was lightly ground in a pestle and mortar, and placed in an airtight sample holder. The airtight sample holder was sealed and placed in a PANanalytical X'Pert pro TTK-450 X-ray Diffractometer, where it was scanned. The duration and the angles of the scan are different for each experiment and will be listed in section 4.

3.6 Packing batteries

To produce a battery, composite electrodes were produced. In a MBRAUN UNIlab glovebox filled with 1 atm argon (Linde), active material, electrolyte $BaSnF_4$, carbon nanofiber and carbon black were weighed on a Sartorius BP301S scale and mixed by hand in a pestle and mortar for 15 minutes. The ratio between the active material, electrolyte, carbon nanofiber and carbon black is different for each instance and listed for all specific experiment descriptions in section 4.

To press the battery, first, an amount of electrolyte was weighed on a Sartorius BP301S scale in a MBRAUN UNIlab glovebox filled with 1 atm argon (Linde). This was, in the glovebox, placed in an electrochemical cell and pressed into a pellet using a Syrio Dental P400 hydraulic press, at a pressure of 240 MPa for 10 minutes. Then, amounts of composite electrode were weighed on the same scale and placed on top and on the bottom of the pellet in the electrochemical cell. Again, the cell was pressed at 240 MPa in a Syrio Dental P400 hydraulic press for 5 minutes. The amounts of composite electrode and electrolyte weighed for this differed per instance and is listed in the specific descriptions of the experiments in section 4.

3.7 Electrochemical impedance spectroscopy

Electrochemical impedance spectroscopy measurements were performed to find the specific ionic conductivity of materials. To perform these measurements, in a MBRAUN UNIlab glovebox filled with 1 atm argon (Linde), the material was weighed on a Sartorius BP301S scale, and placed in an electrochemical cell. The material was then pressed into a pellet by applying 240 MPa using a Syrio Dental P400 hydraulic press for 10 minutes. The cell was then removed from the glovebox and connected to an Autolab PGSTAT302N potentiostat, where the impedance was measured. Then, the pellet was removed from the cell, and its thickness was measured using a Mitutoyo Digital Thickness Gauge ID-C112B at five different places on the pellet, to find the average thickness of the pellet, which could then be used to calculate the specific ionic conductivity.

3.8 Pressure dependence measurements

The measurements to determine the pressure dependence of the ionic conductivity of materials were done similarly to regular conductivity measurements as in section 3.7. In a MBRAUN UNIlab glovebox filled with 1 atm argon (Linde), the material was weighed on a Sartorius BP301S scale, and placed in an electrochemical cell. The material was then pressed into a pellet by applying 240 MPa using a Syrio Dental P400 hydraulic press for 10 minutes. The cell was then removed from the glovebox and placed on an MP5MD – motorische Präzisionspresse automatic press and connected to an Autolab PGSTAT302N potentiostat. Starting from an applied pressure of 0 kPa, impedance measurements were performed at increasingly high pressures, until such pressures were reached that the resistance started to increase with increasing pressures. Then, the pellet was removed from the cell and its thickness was measured using a Mitutoyo Digital Thickness Gauge ID-C112B at five different places on the pellet, to find the average thickness of the pellet, which can then be used to calculate the specific ionic conductivity for each measurement.

3.9 Thermogravimetric measurement of oxygen content

To deduce the oxygen content of several materials, thermogravimetric analysis was used. An amount of material was weighed on a Sartorius BP301S scale, and placed inside an aluminum crucible. The crucible was then placed in a Nabertherm Program Controller S27 furnace, where it was heated in contact with oxygen until it was assumed to be fully oxidized. XRD measurements, as described in section 3.5, were performed to check whether full oxidation occured. The weight increase was then measured using a Sartorius BP301S scale, and was contrasted with what the weight difference would be after full oxidation of a purely oxygen-free compound. This was then used to deduce the original oxygen content of the material.

4 Results and discussion

Various attempts were carried out to produce Fluoride-ion batteries with the desired characteristics. The initial goal was to reproduce results from literature by assembling a symmetric $Bi; BiF_3|BaSnF_4|Bi; BiF_3$ cell, similar as to reported by Grenier [27]. This could then be used as a baseline result for all subsequent battery attempts.

4.1 First battery attempts

To recreate results from literature, it was chosen to produce a symmetric battery cell as reported by Grenier [27], as a symmetric battery reduces the number of variables, since only the cathodic material was used in such a battery. The battery consists of electrolyte $BaSnF_4$ and an electrode material, which was a composite of BiF_3, Bi powder, the electrolyte $BaSnF_4$, which was added for improved ionic conductivity, and carbon black and carbon nanofiber, which were added for improved electronic conductivity.

4.1.1 $BaSnF_4$ synthesis

$BaSnF_4$ was synthesized using the method described in section 3.2. The specifics are listed in table 2. One cubic barium tin fluoride sample was produced using high-energy ball-milling, which was then split into two samples which were thermally annealed to produce two tetragonal barium tin fluoride samples, one of which was annealed for 1h and one of which was annealed for 8h The samples were labeled JZ-200-1 and JZ-200-2, respectively.

Specifications	JZ-200-1	JZ-200-2
BaF_2 added	1.9991 g	1.9991 g
SnF_2 added	1.7790 g	1.7790 g
Ball-milling used	Yes	Yes
RPM ball-milling	600 rpm	600 rpm
Number of ball-milling cycles	60	60
Cycle duration	10 minutes	10 minutes
Rest between cycles	15 minutes	15 minutes
Weight annealed material	0.9943 g	0.9262 g
Annealing temperature	300 °C	300 °C
Annealing time	1h	8h
Annealing temperature ramp-up time	1h	1h

Table 2: Specifics of $BaSnF_4$ synthesis for sample JZ-200-1 and JZ-200-2

To check whether the desired product, t-$BaSnF_4$ had formed, XRD analysis was performed on both JZ-200-1 and JZ-200-2, using the method described in section 3.5. The specifics are listed in table 3. The results are shown in figure 23 and 24. An XRD analysis was also performed on the cubic $BaSnF_4$ sample, before it was thermally annealed (JZ-100-1). The results for that are shown in figure 22.

Material	JZ-200-1	JZ-200-2	JZ-100-1
Under inert atmosphere	Yes	Yes	Yes
Length measurement	40 minutes	40 minutes	52 minutes
Angle measurement	$2\theta = 5 - 90°$	$2\theta = 5 - 90°$	$2\theta = 10 - 90°$

Table 3: Specifications XRD measurements JZ-200-1 and JZ-200-2

In figure 22, the XRD results clearly show a single phase. There is significant peak broadening, implying a small crystallite size, but from the position and number of the peaks, we can tell the material is a single phase material. The position and number of the peaks also tell us that this material is either cubic $BaSnF_4$ or cubic BaF_2. Both materials have a near identical structure and are difficult to differentiate between using X-ray diffraction. [1][48].

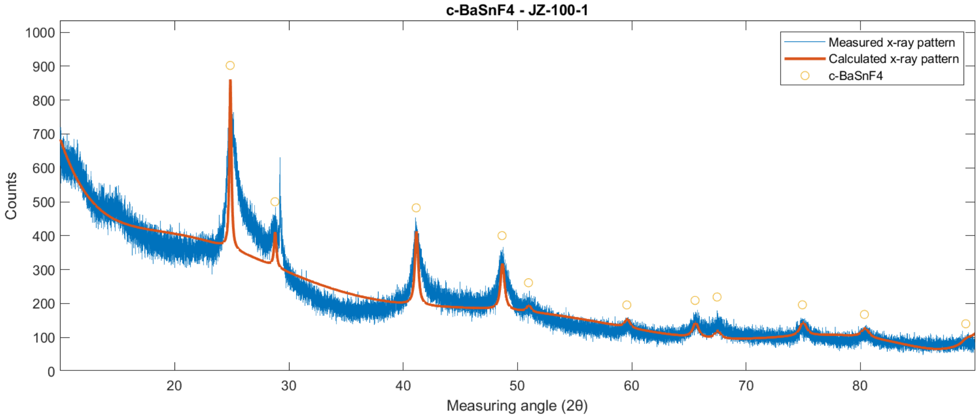

Figure 22: XRD results of JZ-100-1. Rietveld analysis shows cubic barium tin fluoride has formed

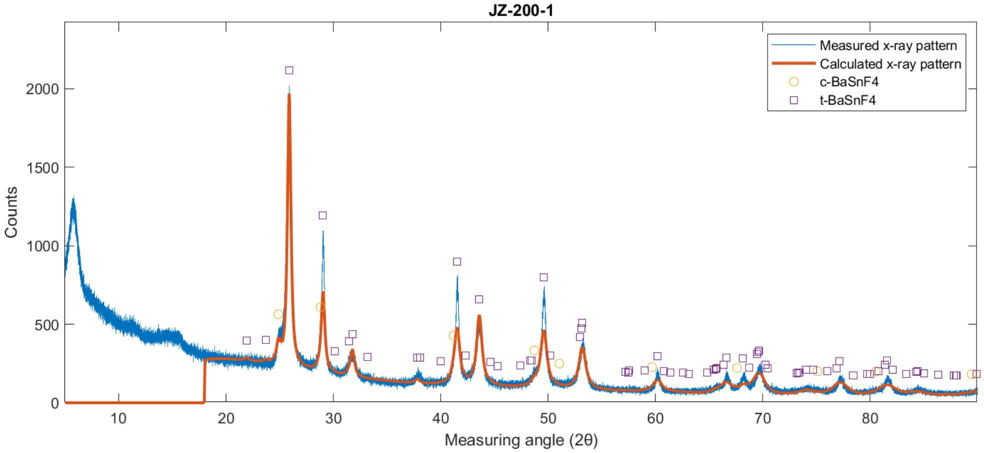

Figure 23: XRD results of JZ-200-1. Rietveld analysis shows a t-$BaSnF_4$ content of 85.4 wt%

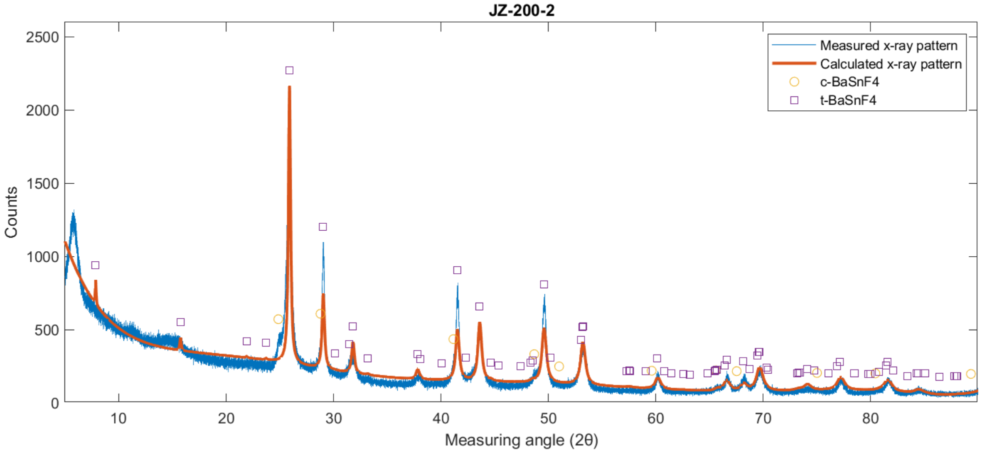

Figure 24: XRD results of JZ-200-2. Rietveld analysis shows a t-$BaSnF_4$ content of 90.0 wt%

Figure 23 and 24 show the XRD results of JZ-200-1 and JZ-200-2 respectively. Both show a material that mainly consists of one phase. However, in the largest peak, at around 26°, in both graphs there is a small shoulder on the peak. This implies the existence of a lesser, secondary phase. From the Rietveld analysis, it was found that the main phase is tetragonal $BaSnF_4$, and the secondary phase was either cubic $BaSnF_4$ or cubic BaF_2. As mentioned above, the structures for cubic $BaSnF_4$ and cubic BaF_2 are very similar and can be difficult to differentiate between.[1][48] These phases are then either the result of an excess of BaF_2 that was mixed with SnF_2, which caused a BaF_2 phase to remain in the material, or the result of not all of the cubic $BaSnF_4$ being converted to tetragonal $BaSnF_4$. Either way, the t-$BaSnF_4$ content of JZ-200-1 and JZ-200-2 was found by the Rietveld analysis to be 85.4 wt% and 90.0 wt% respectively. This was considered to be of sufficient purity to use these materials for subsequent experiments.

4.1.2 Symmetric battery production and testing

A first set of two symmetric fluoride-ion batteries was produced using the procedure detailed in section 3.6. For this, a composite electrode was produced, as detailed in table 4, which was labeled JZ-300-3. The specifications for the production of the batteries are listed in table 5.

Material	Weight
$BaSnF_4$ JZ-200-2	49.7 mg
BiF_3 (Sigma Aldrich, 99.99%)	22.4 mg
Bi powder (Alfa Aesar, 99.5%)	19.3 mg
Carbon black (Cabot, (TOADD: PURITY 9))	5.1 mg
Carbon nanofibers (Aldrich, >98%)	5.2 mg

Table 4: Composition of JZ-300-3 composite electrode material

Specifications	Battery 1	Battery 2
Electrolyte used	JZ-200-2	JZ-200-2
Electrolyte weight	201.2 mg	170.6 mg
Electrode used	JZ-300-3	JZ-300-3
Electrode weight top	10.8 mg	8.7 mg
Electrode weight bottom	17.7 mg	15.0 mg

Table 5: Specifics of the first two symmetric fluoride-ion batteries produced

The batteries were then attached to a MACCOR 4000a Automated Test System, where they would have a constant current of 4.5 μA (5.7 μA cm^{-2}) applied to them until they reached 1 V, and then have a current of -4.5 μA (-5.7 μA cm^{-2}) applied to them until they reached -1 V, which would be repeated for 10 cycles.

Neither measurement yielded any sufficient result. The voltage of each battery did not increase by any significant amount, and no significant amount of capacity was measured.

4.1.3 Non-symmetric battery production and testing

Thereafter, two non-symmetric $BiF_3|BaSnF4|Zn$ batteries were produced, similar to those created by Wang [51]. Again, the procedure detailed in section 3.6 was used. To produce these batteries, first a cathodic and anodic mixture were made, with the materials listed in table 7. The materials used to make the batteries are listed in table 8. The composite cathode material was labeled JZ-300-4 and the composite anode material JZ-400-1. The t-$BaSnF_4$ sample PG-100-7 was used in these batteries. To make this electrolyte, the procedure in section 3.2 was used. The specifics for this are listed in table 6.

Specifications	**PG-100-7**
BaF_2 added	2.0 g
SnF_2 added	1.79 g
Ball-milling used	No
Annealing temperature step 1	250 °C
Annealing time step 1	8h
Annealing temperature ramp-up time step 1	1h
Annealing temperature step 2	500 °C
Annealing time step 2	1h
Annealing temperature ramp-up time step 2	1h

Table 6: Procedure to produce t-$BaSnF_4$ sample PG-100-7

Material	**JZ-300-4**	**JZ-400-1**
$BaSnF_4$ PG-100-7	253.3 mg	204.0 mg
BiF_3 (Sigma Aldrich, 99.99%)	203.5 mg	-
Zn powder (Alfa Aesar, 97.5%)	-	249.8 mg
Carbon black (Cabot, (TOADD: PURITY 9))	37.2 mg	50.4 mg
Carbon nanofibers (Aldrich, >98%)	12.8 mg	-

Table 7: Composition of JZ-300-4 and JZ-400-1 composite electrode material

Specifications	**Battery 1**	**Battery 2**
Electrolyte used	PG-100-7	PG-100-7
Electrolyte weight	251.0 mg	255.7 mg
Electrode used top	JZ-300-4	JZ-300-4
Electrode weight top	15.2 mg	14.6 mg
Electrode used bottom	JZ-400-1	JZ-400-1
Electrode weight bottom	26.9 mg	29.7 mg

Table 8: Specifics of the first two symmetric fluoride-ion batteries produced

Both cells were attached to a MACCOR 4000a Automated Test System battery cycler, where they would have a constant current of 4.5 μA (5.7 μA cm^{-2}) applied to them until they reached 1 V, and then have a current of -4.5 μA (-5.7 μA cm^{-2}) applied to them until they reached -1 V, which would be repeated for 10 cycles.

Just as the batteries in section 4.1.2, the results of these batteries was that there was no significant increase in the voltage or a significant capacity measured. The measurement therefore did not complete.

4.1.4 Discussion

With both the symmetrical and the non-symmetrical batteries failing to yield any significant results, possible issues need to be analyzed to figure out how to produce a working battery.

One possible such issue was the pressure retention of the batteries. The battery pellets were pressed at 140 to 240 MPa. When this same type of cell was used to measure ionic conductivity of materials in this manner, a loss of ionic conductivity was noticed over time, as will be detailed in subsection 4.2.1. This was hypothesized to be the result of the cell losing pressure over time. The effect of differences of pressure on the ionic conductivity of the cathodic and electrolyte material are analyzed in section 4.2

Another possible cause for this was hypothesized to be the purity of the materials used to create this battery. The materials therefore had their oxygen content measured. This is performed in section 4.3.

4.2 Conductivity dependence on pressure

4.2.1 Conductivity decay over time

To show the effect of pressure loss over time on the ionic conductivity, a time-dependent conductivity measurement was performed. The procedure detailed in section 3.7 was followed. When the pressure was removed from the cell, the time was recorded and 50 impedance measurements were performed after specific times after the release of the pressure. The details of the measurement are shown in table 9. The results from the EIS measurements are shown in figure 25 and 26. These figures clearly show a sharp decrease in ionic conductivity over time, which points to the conclusion that a loss of pressure on the cell causes a decrease in conductivity.

t-$BaSnF_4$ sample used	PG-100-7
Weight sample	220.3 mg
Average thickness pellet	0.6028 mm
Measured thicknesses pellet	0.592 mm 0.594 mm 0.609 mm 0.608 mm 0.611 mm

Table 9: Specifics of time-dependent EIS measurements

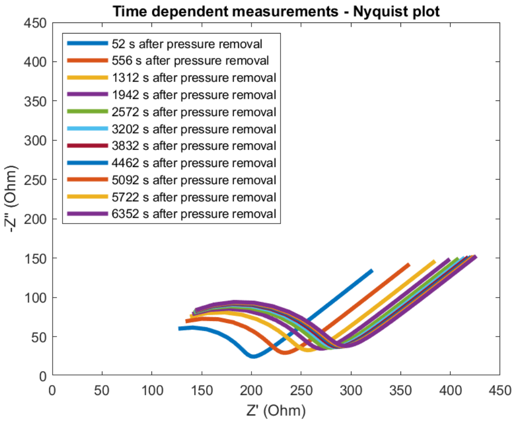

Figure 25: Effect of time passed on the ionic conductivity of $BaSnF_4$ - Nyquist plots

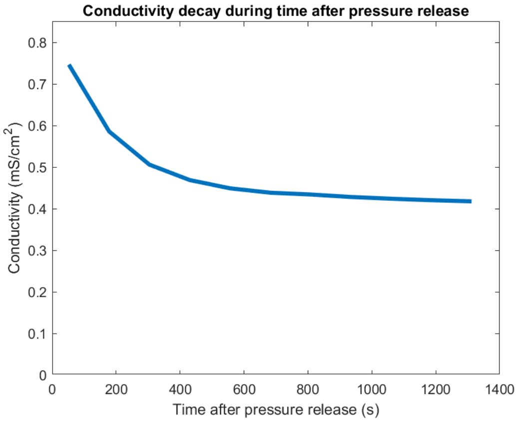

Figure 26: Effect of time passed on the ionic conductivity of $BaSnF_4$ - conductivity plotted against time

Now that we've shown a clear decrease in ionic conductivity over time, we will analyze the effect of decreasing pressure on the ionic conductivity of both $BaSnF_4$ and BiF_3, which will be detailed in subsection 4.2.2 and 4.2.3 respectively. No measurements have been reported in literature for the behaviour of the ionic conductivity under different pressures for these specific materials as of yet.

4.2.2 $BaSnF_4$ ionic conductivity dependence on pressure

To analyze the effect of the pressure on the ionic conductivity of $BaSnF_4$, pressure dependence measurements as detailed in section 3.8 were performed, using the specifics outlied in table 10. The results are detailed in figure 27 and 28.

t-BaSnF$_4$ sample used	JZ-200-1
Weight sample	202.4 mg
Average thickness pellet	0.709 mm
Measured thicknesses pellet	0.709 mm 0.716 mm 0.725 mm 0.701 mm 0.694 mm

Table 10: Specifics of BaSnF$_4$ pressure dependence ionic conductivity measurements

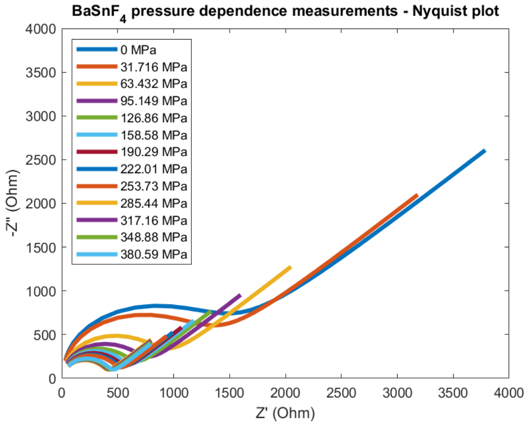

Figure 27: Effect of different pressures on the ionic conductivity of BaSnF$_4$ - Nyquist plots

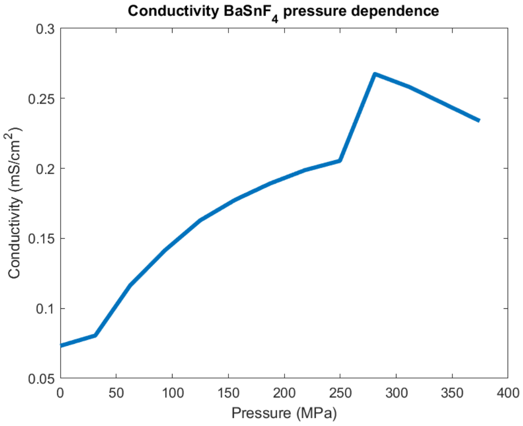

Figure 28: Effect of pressure on the ionic conductivity of BaSnF$_4$ - conductivity plotted vs pressure

These figures show how the ionic conductivity of BaSnF$_4$ increases sharply with increasing pressure, until they reach roughly 380 MPa, at which point the ionic conductivity starts to decrease with increasing pressure.

4.2.3 BiF$_3$ conductivity dependence on pressure

Similar measurements have been carried out for BiF$_3$. The procedure outlined in section 3.8 was followed. The specifics are detailed in table 11. The results are detailed in figure 29 and figure 30.

BiF$_3$ sample used	FluoroChem (99%)
Weight sample	326.3 mg
Average thickness pellet	0.5762 mm
Measured thicknesses pellet	0.540 mm 0.513 mm 0.540 mm 0.596 mm 0.555 mm

Table 11: Specifics of BiF$_3$ pressure dependence conductivity measurements

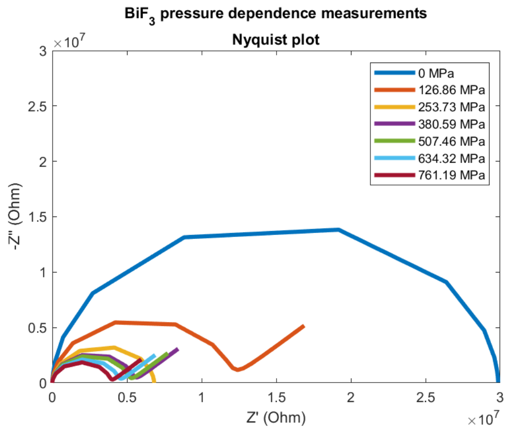

Figure 29: Effect of different pressures on the ionic conductivity of BiF$_3$ - Nyquist plot. For the sake of visibility, the plot shows only the Nyquist plots for every fourth measurement.

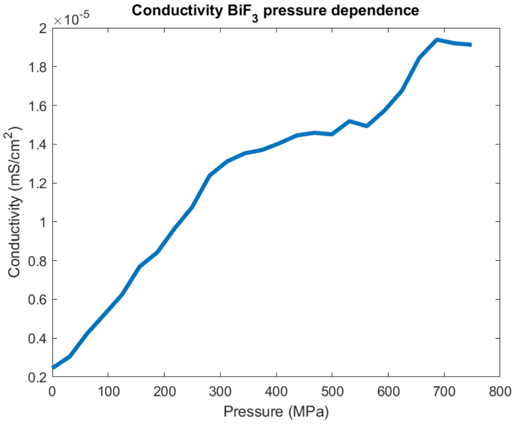

Figure 30: Effect of different pressures on the ionic conductivity of BiF$_3$ - conductivity plotted vs pressure

These figures show how the ionic conductivity of BiF$_3$ sharply increases with pressure, until it reaches pressures of around 700 MPa, at which point it starts decreasing.

Figure 28 and figure 30, which show the ionic conductivity behaviour under different pressures of BaSnF$_4$ and BiF$_3$ respectively, undergo a similar behaviour. Both materials initially experience a sharp increase in ionic conductivity with an increase in pressure, which then at higher pressures level out somewhat. Then, at higher pressures still, both materials experience another sharp increase in ionic conductivity, before the ionic conductivity starts decreasing. This two-step increase in the ionic conductivity follows a similar pattern for both materials and is not seen in other examples of conductivity dependence on pressure, as seen for example in figure 17 and 18. It should be noted that this happened at different pressures, with the second ionic conductivity increase step occuring at around 250 MPa for BaSnF$_4$ and around 600 MPa for BiF$_3$. Therefore, it should be concluded that this effect cannot be explained by effects of the equipment used for these measurements, and could instead be caused by an effect that is intrinsic to each material.

4.3 Measuring oxygen content of materials used

As the batteries in section 4.1 were not producing any significant capacity, one of the hypotheses for this issue was that the materials used to construct these batteries were not pure enough. Since nearly all materials used in these batteries are sensitive to oxygen, the most likely type of impurity was oxides. It was hypothesized that presence of oxides in the material could affect the ionic conductivity of the materials which could impede transport of ions to the cathode and anode materials. To this end, four materials needed to be tested for oxides: BiF$_3$, BaSnF$_4$, Bi powder and Zn powder.

4.3.1 Bismuth powder oxygen content

To check the oxygen content of bismuth powder, a thermogravimetric analysis was performed similar as was performed by Grenier[28]. The procedure followed for this is described in section 3.9. The details are shown in table 13.

Material	Bi powder - oxidized	Bi powder - pre-oxidation
Under inert atmosphere	No	Yes
Length measurement	170 minutes	91 minutes
Angle measurement	$2\theta = 10 - 90°$	$2\theta = 10 - 90°$

Table 12: Oxidized bismuth powder and pre-oxidation bismuth powder XRD measurement specifics

Bismuth sample	Alfa Aesar, 99.5%
Weight sample	1.2434 g
Weight after annealing	1.2958 g
Annealing temperature	300 °C
Annealing time	12 h
Annealing temperature ramp-up time	1h

Table 13: Thermogravimetric analysis of bismuth powder oxygen content

To check whether the substance had been fully oxidized, an XRD-scan was performed on the material, as described in section 3.5. The details are listed in table 12. The results are shown in figure 32. An XRD-scan was also performed on the bismuth powder prior to the oxidation. This is shown in figure 31.

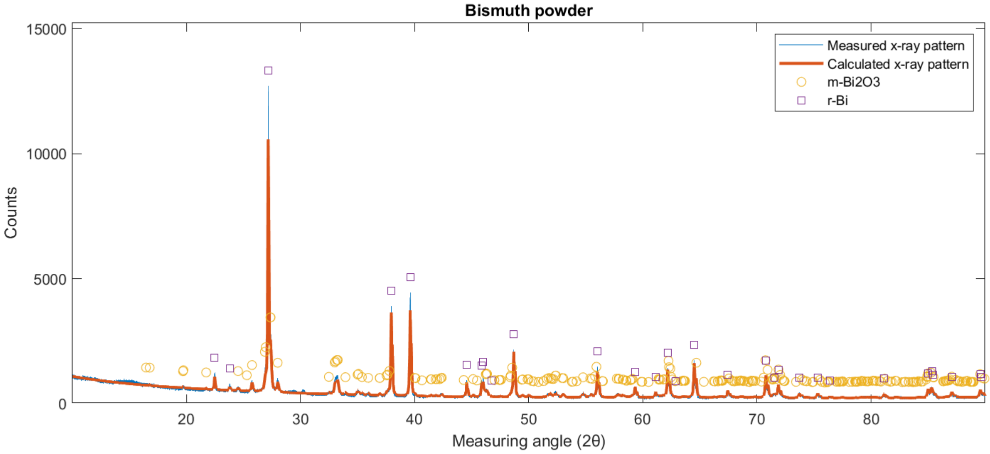

Figure 31: XRD scan of the bismuth powder prior to the oxidation.

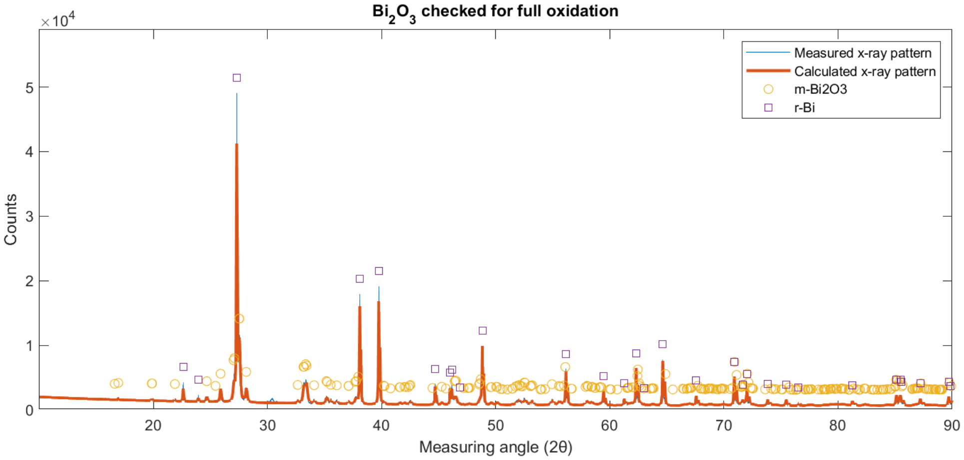

Figure 32: XRD measurements to check whether Bismuth was fully oxidized

Figure 32 shows the results from the XRD scan. While most of the bismuth had indeed been oxidized, it still shows a bismuth metal component of 7.6 wt%. Since no full oxidation was realized, this measurement cannot give a precise answer to the oxygen content in the bismuth powder sample. However, a rough indication can be made. The weight of the bismuth precursor increased from 1.2434 g to 1.2958 g. A content of 7.6 wt% of bismuth metal is equal to 0.076 * 1.2958 g = 0.0985 g bismuth metal which did not take part in the oxidation reaction. This means a total of 1.2434 g - 0.0985 g = 1.1449 g of initial bismuth precursor, when oxidized fully, weighed 1.2958 g - 0.0985 g = 1.1973 g. 1.1973 g of Bi_2O_3 is equal to 1.1973 g / 465.96 g/mol = 2.570 mmol Bi_2O_3. A weight gain of 1.1973 g - 1.1449 g = 0.0524 g of O atoms added to the compound. 0.0524 g O atoms is equal to 0.0524 g / 15.999 g/mol = 3.28 mmol O atoms. Since during oxidation, 1.5 O atom is added to every Bi atom, the amount of bismuth atoms oxidized during this reaction is 3.28 mmol / 1.5 = 2.18 mmol Bi. This means 2.57 - 2.18 = 0.39 mmol of Bi was not oxidized during this reaction, meaning that amount of Bi was already oxidized prior to the reaction. This means a total of 0.39 mmol * 465.96 g/mol = 181.7 mg of Bi_2O_3 was present in the original 1.2434 g, so a wt% of 14.6%. To reiterate, due to the combined inaccuracies of the thermogravimetric analysis and the Rietveld refinement of the XRD measurement, this is not a fully reliable value, but it does give a solid indication that the oxide content of the bismuth powder is larger than would be desirable.

4.3.2 Zinc powder oxygen content

Zinc powder was similarly analysed using thermogravimetric analysis. The procedure followed for this is described in section 3.9. The details are shown in table 14.

Zinc sample	Alfa Aesar, 97.5%
Weight sample	1.9769 g
Weight after annealing	2.2185 g
Annealing temperature	375 °C
Annealing time	14 h
Annealing temperature ramp-up time	1h

Table 14: Thermogravimetric analysis of zinc powder oxygen content

To check whether the substance had been fully oxidized, an XRD-scan was performed on the material, as described in section 3.5. The details are listed in table 15. The results are shown in figure 33.

Under inert atmosphere	No
Length measurement	51 minutes
Angle measurement	$2\theta = 10 - 90°$

Table 15: Oxidized zinc powder XRD measurement specifics

Rietveld refinement of this XRD data showed that the sample contained 5.4 wt% of Zn metal. This means that similar to the bismuth metal in section 4.3.1, the powder was not fully oxidized, and although the results can still be used to calculate the initial ZnO content, the results will be less accurate. The weight of the zinc precursor increased from 1.9769 g to 2.2185 g. A content of 5.4 wt% of zinc metal is equal to 0.054 * 2.2185 g = 0.1198 g zinc metal which did not take part in the oxidation reaction. This means a total of 2.2185 g - 0.1198 g = 2.0987 g of initial Zn precursor, when oxidized fully, weighed 1.9769 g - 0.1198 g = 1.8571 g. 1.8571 g of ZnO is equal to 1.8571 g / 81.38 g/mol = 22.82 mmol ZnO. A weight gain of 2.2185 g - 1.9769 g = 0.2416 g of O atoms added to the compound. 0.2416 g O atoms is equal to 0.2416 g / 15.999 g/mol = 15.11 mmol O atoms. Since during oxidation, one O atom is added per Zn atom, the amount of zinc atoms oxidized during this reaction is also equal to 15.11 mmol. This means 22.82 mmol - 15.11 = 7.71 mmol of Zn was not oxidized during this reaction, meaning that amount of Zn was already oxidized prior to the reaction. This means a total of 7.71 mmol * 81.38 g/mol = 627.4 mg of ZnO was present in the original 1.9769 g, so a wt% of 31.7%. As stated previously, due to the combined inaccuracies of the thermogravimetric analysis and the Rietveld refinement of the XRD measurement, this is not a fully reliable value, but it does give a solid indication that the oxide content of the zinc powder is larger than would be desirable.

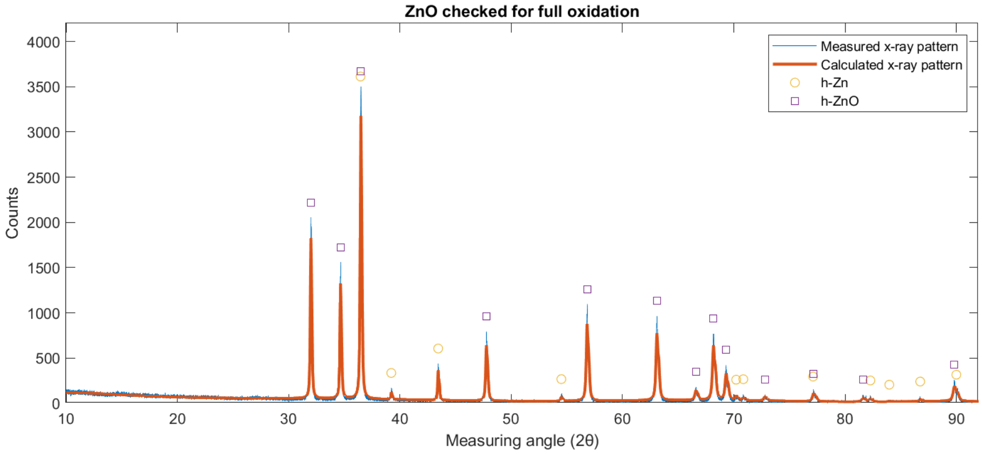

Figure 33: XRD measurements to check whether Zinc was fully oxidized

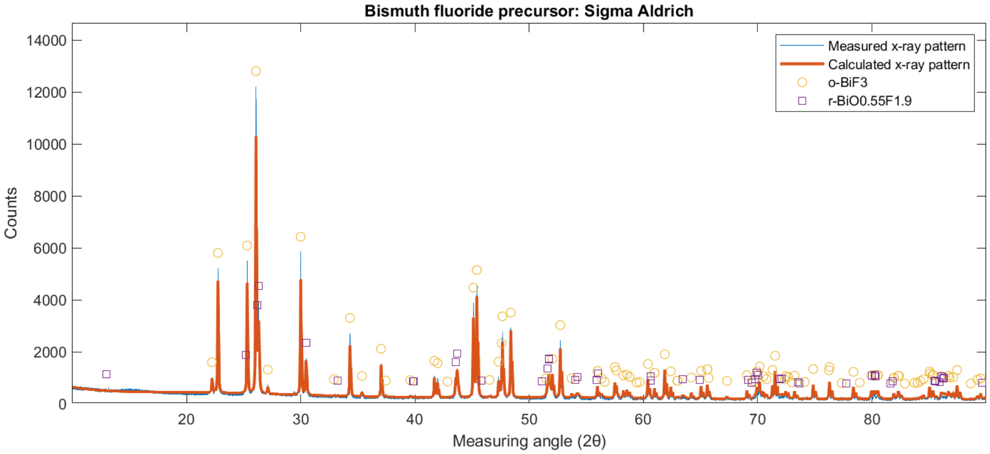

Figure 34: XRD measurement to check for oxygen impurities

4.3.3 BiF_3 and $BaSnF_4$ oxygen content

Since the reaction to oxidize BiF_3 and $BaSnF_4$ is much less simple than for Bi powder and Zn powder, a thermogravimetric analysis was not performed on these materials. Instead, the materials were simply analyzed using X-ray diffraction. Figure 23 and 24 already showed the XRD analysis of the produced $BaSnF_4$, and the Rietveld refinement showed no significant amount of oxides present in either sample. This $BaSnF_4$ was thus considered pure enough to use to produce batteries. The BiF_3 precursor is analyzed in this section.

To analyze the BiF_3 precursor, an XRD scan was performed, as outlined in section 3.5. The details are shown in table 16. The results are shown in figure 34.

Under inert atmosphere	Yes
Length measurement	52 minutes
Angle measurement	$2\theta = 10 - 90°$

Table 16: BiF_3 (Sigma Aldrich, 99.99%) XRD measurement to check for oxygen content

The Rietveld refinement for this XRD scan showed a $BiO_{0.55}F_{1.9}$ content of 17.5 wt% which is a significant amount of oxygen present in the material. It is thought that this large amount of oxygen might be the cause of the batteries in section 4.1 not producing significant results.

From this point, a new research questions emerged: whether the presence of significant amounts of oxygen in BiF_3 affects the ionic conductivity of the material and subsequently the battery performance. The effect of oxygen impurities on the ionic conductivity of the cathodic material was analyzed.

4.4 Conductivity dependence on oxygen present in BiF_3

Note: The following section was carried out by Tim Middendorp, Lucas van der Poll and Jordy Frenk under my supervision as part of a project in their minor program Modern Physics.

Since oxygen impurities were found to exist in the precursor materials for the Fluoride-ion batteries, the question emerged what effect these impurities can have on the ionic conductivity of the material. To this end the following materials were synthesized:

- h-BiF_3 (75% fluoride)
- $Bi_7O_9F_3$ (∼16% fluoride)
- BiOF (∼33% fluoride)
- $Bi_7O_5F_{11}$ (∼48% fluoride)
- Bi_2OF_4 (∼57% fluoride)

These materials were chosen as they are all known to be stable at room temperature, as documented by Springer Materials[86] and shown in figure 35. This figure shows the phase diagram of Bi-O-F compounds, where all the sections in purple correspond to a stable phase existing at that composition and temperature. At high temperatures, mostly above 400°C, a wide range of different Bi-O-F compounds were found to be stable. However, at low temperatures, below 100°C, the number of stable Bi-O-F compounds is much lower. The only compounds found to be stable under these conditions were: Bi_2O_3, $Bi_7O_9F_3$, BiOF, $Bi_7O_5F_{11}$, $Bi_5O_3F_9$, $BiO_{0.55}F_{1.90}$, $BiO_{0.52}F_{1.96}$, Bi_2OF_4 and BiF_3. The materials listed were chosen as they represented a broad range of different oxygen to fluoride ratios.

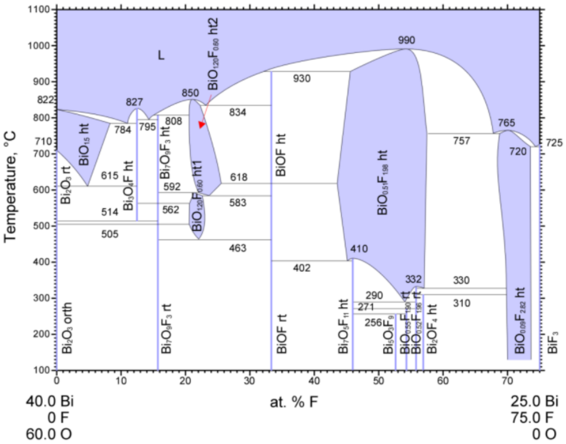

Figure 35: Phase diagram of possible Bi-O-F compounds.[86]

After synthesis, all the listed materials had their ionic conductivity measured. They were also analyzed using X-ray Diffraction to check whether the attempted product had indeed been synthesized.

4.4.1 Synthesis of Bi-O-F compounds

For the synthesis of these materials, the steps described in section 3.3 were followed. The details are shown in table 17.

Material	**Weight BiF_3**	**Weight Bi_2O_3**	**Annealing temperature**	**Annealing time**	**Ramp-up time**
h-BiF_3	2160.5 mg	-	700 °C	13 h	1 h
Bi_2OF_4	694.4 mg	305.9 mg	700 °C	13 h	1 h
$Bi_7O_5F_{11}$	552.7 mg	453.1 mg	700 °C	13 h	1 h
BiOF	360.1 mg	453.1 mg	700 °C	13 h	1 h
$Bi_7O_9F_3$	160.7 mg	841.6 mg	700 °C	13 h	1 h

Table 17: Specifications of the synthesis of Bi-O-F compounds

4.4.2 XRD analysis of Bi-O-F compounds

Of the samples produced in the previous section, all but the h-BiF_3 sample were analyzed using X-ray diffraction to check whether the desired compound had been produced. For this the procedure described in section 3.5 was followed, the details of which are shown in table 18. The results of these scans are shown in figures 37, 38, 39 and 40.

Material	Under inert atmosphere	Length measurement	Angle measurement
Bi_2OF_4	Yes	29 minutes	$2\theta = 10 - 90°$
$Bi_7O_5F_{11}$	Yes	29 minutes	$2\theta = 10 - 90°$
BiOF	Yes	29 minutes	$2\theta = 10 - 90°$
$Bi_7O_9F_3$	Yes	29 minutes	$2\theta = 10 - 90°$

Table 18: Specifications of Bi-O-F material XRD scans

Figure 38 and 39 show the XRD results of BiOF and $Bi_7O_5F_{11}$ respectively. The BiOF sample shows a single phase material, with the peaks neatly corresponding to those that would be expected for BiOF. The $Bi_7O_5F_{11}$ sample contains one major phase which corresponds to the expected peaks for that material, with a minor phase of BiOF also present. The Rietveld refinement shows that around 80% of the sample contains $Bi_7O_5F_{11}$. The results for the Bi_2OF_4 and $Bi_7O_9F_3$ compounds, shown in figure 40 and 37 respectively, are somewhat more complicated. Neither of those materials exist in the database used for Rietveld refinement, and therefore the refinement wasn't able to find an adequate match. For the Bi_2OF_4 compound, the materials c-$BiO_{0.51}F_{1.98}$ and r-$BiO_{0.55}F_{1.90}$ were detected. Both have nearly the same composition as Bi_2OF_4. Due to the similarity between c-$BiO_{0.51}F_{1.98}$ and r-$BiO_{0.55}F_{1.90}$, the Rietveld refinement may not have been able to tell them apart. Since one material is cubic, and the other is rhombohedral, a distinction can be made by looking at the peaks caused by the (111), (311) and (420) faces. These peaks appear at an angle of $2\theta \approx 26°, 52°$ and $73°$. A zoomed in graph is shown in figure 36. Here it is clear that there is splitting in these peaks, and thus the rhombohedral material r-$BiO_{0.55}F_{1.90}$ is likely present. For the material $Bi_7O_9F_3$, no closely related match could be found.

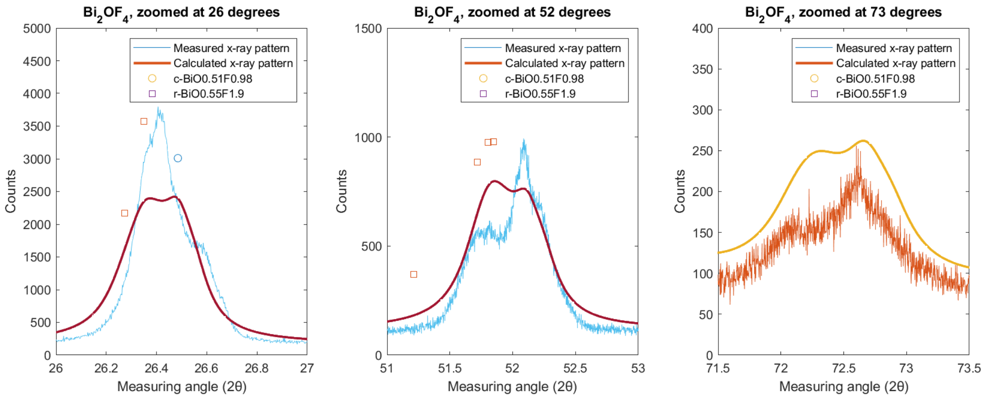

Figure 36: XRD scan of the synthesized Bi_2OF_4 compound, zoomed in on the peaks at 26, 52 and 72 degrees.

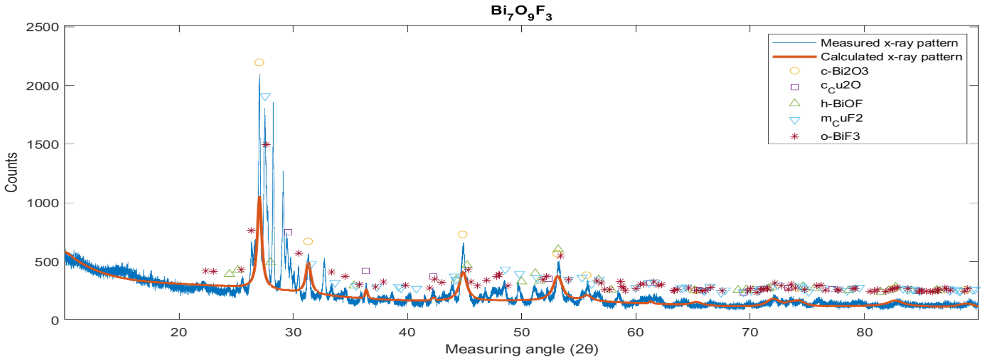

Figure 37: XRD scans of the synthesized $Bi_7O_9F_3$ compounds

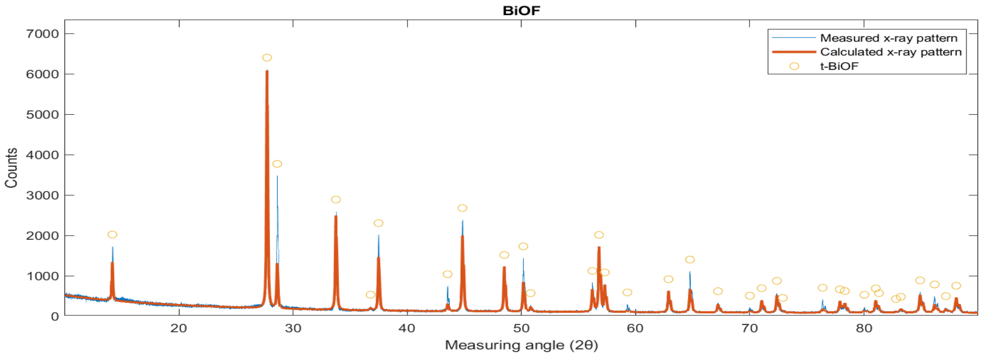

Figure 38: XRD scans of the synthesized $BiOF$ compounds

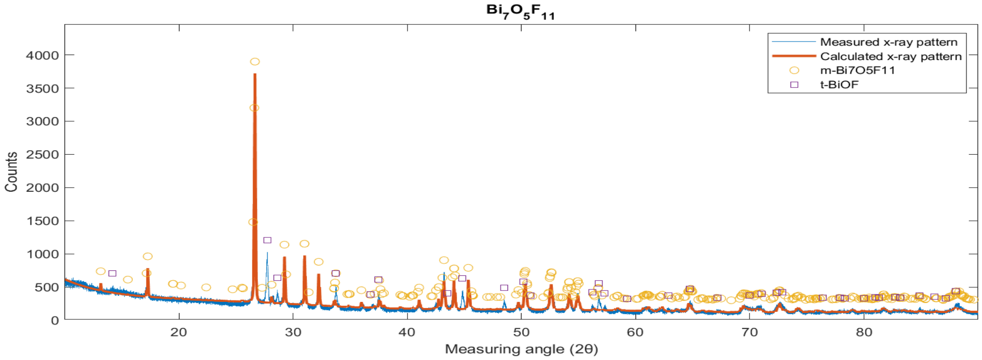

Figure 39: XRD scans of the synthesized $Bi_7O_5F_{11}$ compounds

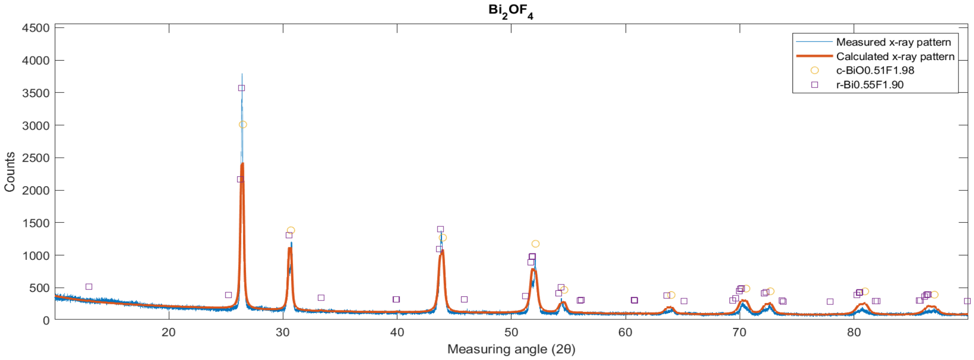

Figure 40: XRD scans of the synthesized Bi_2OF_4 compounds

4.4.3 Conductivity of Bi-O-F compounds

Each of the materials has had its ionic conductivity measured using Electrochemical Impedance Spectroscopy (EIS). For each compound, the steps in section 3.7 were followed. The results are listed in table 19. The results are also shown in figure 41, 42, and 43.

Sample	x1	x2	x3	x4	x5	x_{av}	Resistance	Conductivity
BiF_3	0.406 mm	0.530 mm	0.514 mm	0.437 mm	0.468 mm	0.471 mm	16889 Ω	0.0035508 mS/cm^1
Bi_2OF_4	0.413 mm	0.444 mm	0.417 mm	0.463 mm	0.471 mm	0.4416 mm	$3.43{*}10^7\Omega$	$1.6392 *10^{-6}$ mS/cm^1
$Bi_7O_5F_{11}$	0.457 mm	0.416 mm	0.456 mm	0.429 mm	0.451 mm	0.4418 mm	$3.36{*}10^8\Omega$	$1.6742{*}10^{-7}$ mS/cm^1
BiOF	0.510 mm	0.401 mm	0.544 mm	0.440 mm	0.510 mm	0.481 mm	$1.25{*}10^7\Omega$	$4.8994{*}10^{-6}$ mS/cm^1
$Bi_7O_9F_3$	0.415 mm	0.413 mm	0.437 mm	0.462 mm	0.395 mm	0.4244 mm	$1.81{*}10^7\Omega$	$2.9854{*}10^{-6}$ mS/cm^1

Table 19: Results from the Bi-O-F compound conductivity measurements

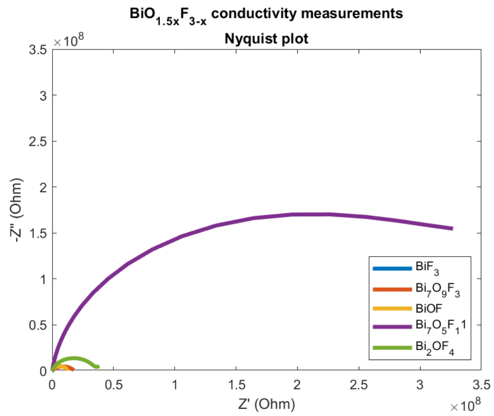

Figure 41: Nyquist plots for synthesized Bi-O-F compounds

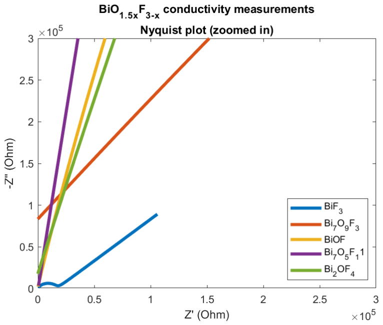

Figure 42: Nyquist plots for synthesized Bi-O-F compounds, zoomed in to see the ionic conductivity of BiF_3

As can be seen from these results, the presence of oxygen significantly decreases the ionic conductivity, as compared to pure BiF_3. There seems to be no direct link between the amount of oxygen and the ionic conductivity, but all oxygen-containing compounds have a much higher resistivity than the pure BiF_3 compound, having an ionic conductivity that is a factor 10^5 to 10^8 lower. Given that quite a considerable amount of oxygen was present in the BiF_3 precursor used in section 4.1 to make batteries, it is plausible that the added resistance from these oxides are the reason the batteries failed to yield significant results.

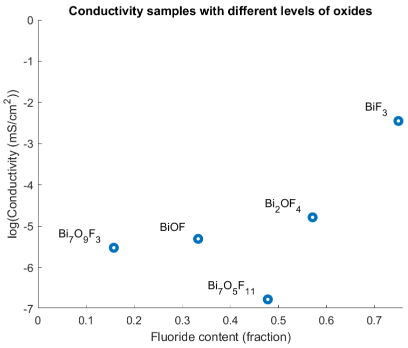

Figure 43: Ionic conductivity of synthesized Bi-O-F compounds

4.5 Conductivity dependence on tin doping

Note: The following section was carried out by Tim Middendorp, Lucas van der Poll and Jordy Frenk under my supervision as part of a project in their minor program Modern Physics.

4.5.1 Synthesis of tin-doped BiF_3

Now that it is clear that the cathodic material used in batteries produced in section 4.1 contained significant amount of oxides, as shown in section 4.3 and that oxides drastically reduce the ionic conductivity of the material as shown in section 4.4.2, it is deemed plausible that the reduction in ionic conductivity caused by the oxides present may have contributed to the batteries failing to yield significant results. Because of these observations, another research question emerges: can a cathodic material that is modified to have improved ionic conductivity also improve the behaviour of the battery?

One possibility for improving the ionic conductivity of bismuth fluoride, is by doping it with tin fluoride. Since tin fluoride is bivalent as opposed to the trivalent bismuth fluoride, doping with tin fluoride will leave vacancies which, it is theorized, can improve the ionic conductivity of the fluoride ions. In 2015, the group of Pei released a paper that used first principle calculations to find that doping BiF_3 with tin fluoride indeed can lead to improved ionic conductivity.[95] Here, we attempt to study this in practice.

Several different concentrations of tin-doped bismuth fluoride ($Bi_{1-x}Sn_xF_{3-x}$) were synthesized, with x = 0.00, 0.05, 0.10, 0.15, 0.20. These have all had their ionic conductivity measured using Electrochemical Impedance Spectroscopy and were also analyzed using X-ray Diffraction to check whether the desired material was produced.

For the synthesis of these materials, the steps in section 3.4 were followed. The specifics for this are listed in table 20.

wt% Sn	**Weight BiF_3**	**Weight SnF_2**	**Annealing temperature**	**Annealing time**	**Ramp-up time**
0%	991.4 mg	-	700 °	13 h	2 h
5%	967.2 mg	33.0 mg	700 °	13 h	2 h
10%	934.3 mg	62.1 mg	700 °	13 h	2 h
15%	905.3 mg	93.9 mg	700 °	13 h	2 h
20%	871.8 mg	127.6 mg	700 °	13 h	2 h

Table 20: Specifics of tin-doped bismuth fluoride production

4.5.2 XRD analysis of tin-doped BiF_3

The sample that was doped with 10% SnF_2 was analyzed using X-ray diffraction, to check whether the desired product was produced. The procedure outlined in section 3.5 was followed, using the specifics listed in table 21. The results are shown in figure 44.

Inert atmosphere	Yes
Time measurement	42 minutes
Angle measurement	$2\theta = 10 - 90°$

Table 21: XRD measurement of tin-doped BiF_3 specifics

The Rietveld refinement of this XRD scan found that a hexagonal BiF_3 material was present in the sample. Hexagonal BiF_3 does not exist in pure form. BiF_3 can only exist as a hexagonal phase if it is stabilized by vacancies caused by dopants [54]. The Rietveld refinement software assigned those vacancies to be caused by oxygen, but tin-doped BiF_3 was here not considered as an option as it does not exist in the software's database. From the lattice parameters, we see that the structure is

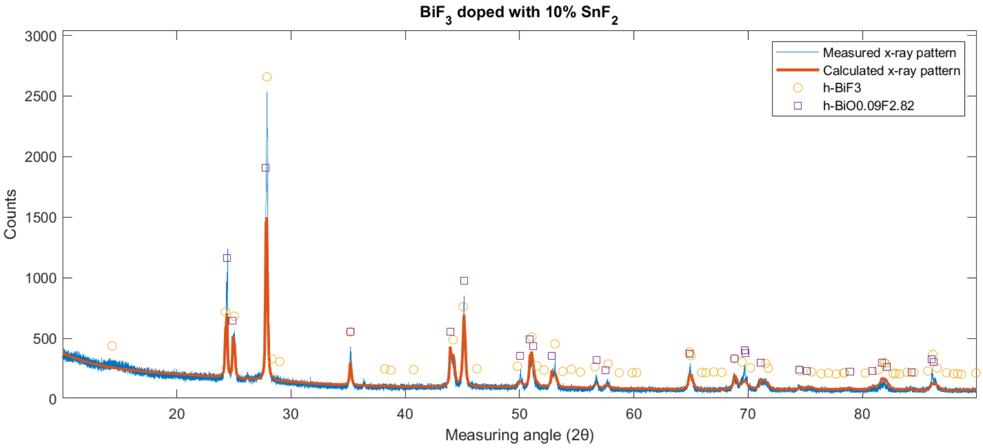

Figure 44: XRD scan of the BiF$_3$ sample doped with 10% SnF$_2$

somewhat larger in size, compared to the values expected for BiO$_{0.09}$F$_{2.82}$, having lattice parameters of a and b = 4.11 Å and c = 7.27 Å, whereas for BiO$_{0.09}$F$_{2.82}$ this was expected as a and b = 4.09 Å and c = 7.27 Å [5]. It is quite plausible that the tin dopants are what is stabilizing the hexagonal phase. Since SnF$_2$ was not found in its pure form, it is assumed the doping has been succesful.

4.5.3 Conductivity of tin-doped BiF$_3$ compounds

All tin-doped BiF$_3$ samples had their ionic conductivity measured using Electrochemical Impedance Spectroscopy, with the exception of the sample doped with 5% SnF$_2$, which had too low of a yield to be used to measure the ionic conductivity. The ionic conductivity of the BiF$_3$ precursor was also measured for comparison. For these materials, the steps outlined in section 3.7 were followed. The results are shown in figure 45 and 46 and listed in table 22

Material	x_1 / mm	x_2 / mm	x_3 / mm	x_4 / mm	x_5 / mm	x_{av} / mm	Resistance	Conductivity
BiF$_3$	0.552	0.556	0.581	0.586	0.596	0.5762	19584	0.00310 mS cm^{-1}
BiF$_3$ with 10% SnF$_2$	0.305	0.535	0.545	0.518	0.483	0.4772	3958.3	0.01853 mS cm^{-1}
BiF$_3$ with 15% SnF$_2$	0.506	0.515	0.492	0.416	0.457	0.4772	28693	0.00212 mS cm^{-1}
BiF$_3$ with 20% SnF$_2$	0.523	0.529	0.560	0.514	0.528	0.5308	16366	0.00413 mS cm^{-1}

Table 22: Results of the EIS measurements of tin-doped BiF$_3$ samples

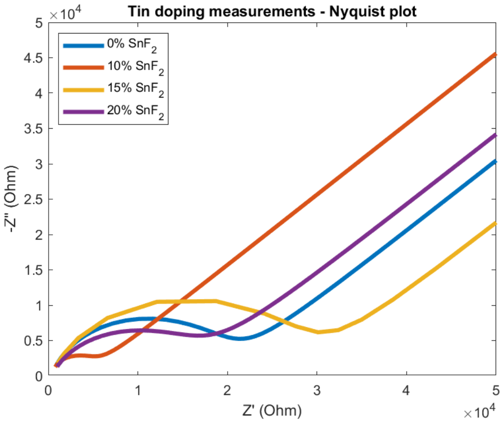

Figure 45: Nyquist plots for synthesized tin-doped compounds

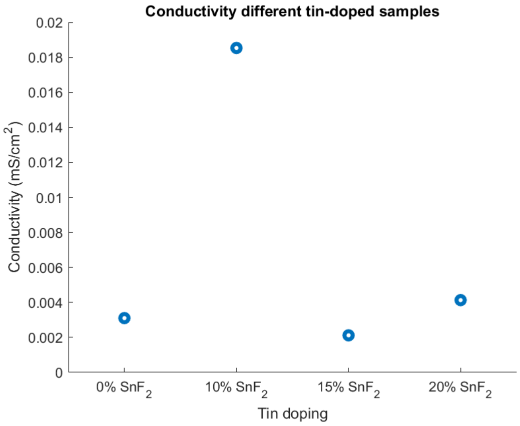

Figure 46: Ionic conductivity of synthesized tin-doped compounds

From these figures, it shows that the highest ionic conductivity can be reached by doping the BiF_3 sample with 10% SnF_2. At doping concentrations higher than 10%, the ionic conductivity again reaches levels close to the ionic conductivity of the pure BiF_3 sample, but the sample doped with 10% SnF_2 showed an ionic conductivity of a factor 5 higher than each of the other samples. This shows that ionic conductivity can indeed be increased by doping with the right amount of SnF_2.

4.6 XRD analysis of new BiF_3 and Bi-powder materials

4.6.1 XRD analysis

For the next attempt to produce fluoride-ion batteries, new materials were used. BiF_3 from two different sources was analyzed using X-ray Diffraction to check for oxide contents. The steps listed in section 3.5 were used for this, using the specifics listed in table 23. The results are shown in figure 47 and 48.

Specifics	BiF_3 (FluoroChem)	BiF_3 (ApolloScientific)	Bi powder (Aldrich)
Inert atmosphere	Yes	Yes	Yes
Time measurement	117 minutes	117 minutes	91 minutes
Angle measurement	$2\theta = 10 - 90°$	$2\theta = 10 - 90°$	$2\theta = 10 - 90°$

Table 23: Specifics of the XRD measurement of the new BiF_3 and Bi powder samples

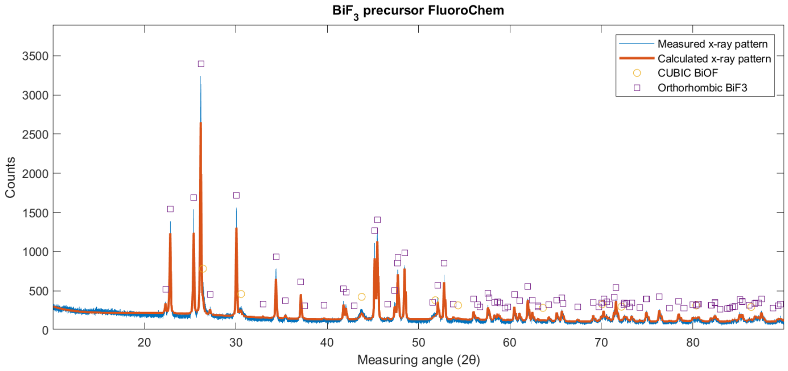

Figure 47: XRD scans of the new bismuth fluoride sample from FluoroChem

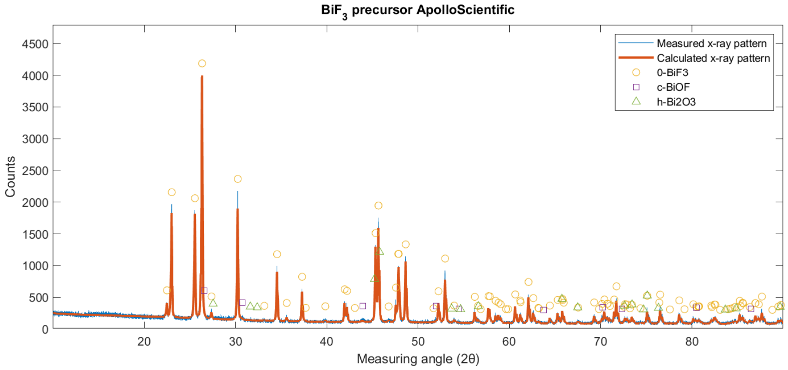

Figure 48: XRD scans of the new bismuth fluoride sample from ApolloScientific

The Rietveld refinement for the Fluorochem sample showed a BiOF content of 7.8 wt%. The Rietveld refinement for the ApolloScientific sample showed no other material present than BiF_3. The BiF_3 sample from ApolloScientific was thus deemed suitable for the next attempt to create fluoride-ion batteries.

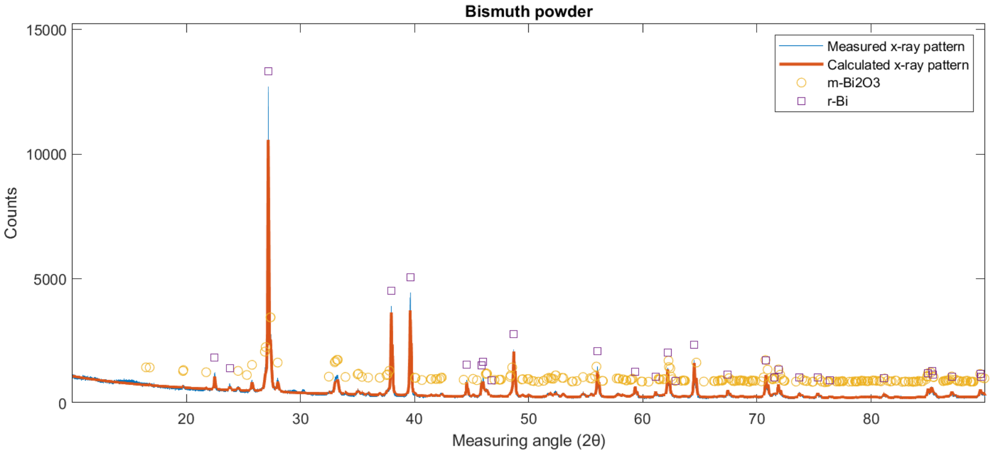

Figure 49: XRD scans of the bismuth powder precursor

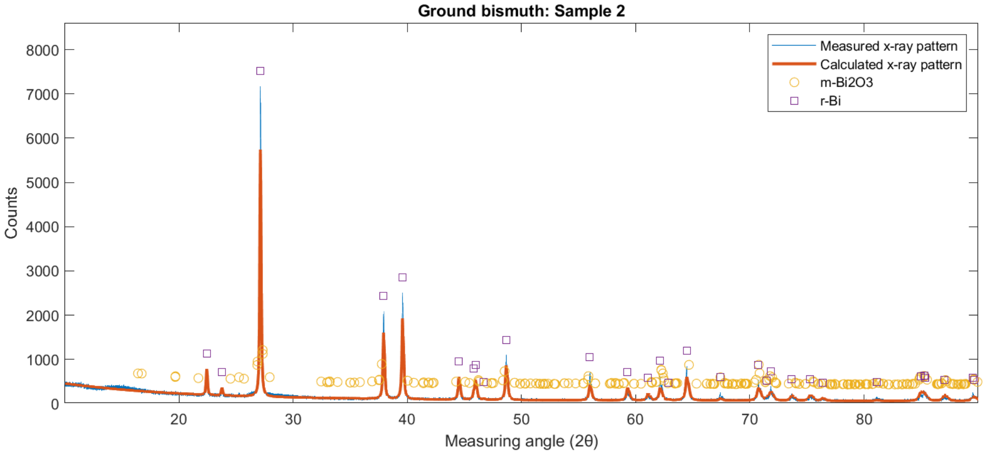

Figure 50: XRD scans of the second ground bismuth sample

For bismuth powder, a new sample was also tested. The procedure from section 3.5 was followed, and the details are also shown in table 23. The results are shown in figure 49.

In the figure, we can see that while a major Bi phase exists, a significant Bi_2O_3 phase is also present. The peak at around 33° is indicative of a Bi_2O_3 phase. The Rietveld refinement found that this bismuth sample contained 33.7 wt% Bi_2O_3, which would negatively affect the battery characteristics, as found in section 4.4.2. Therefore, a new sample was ordered, of bismuth granules.

4.6.2 Grinding of bismuth granules

A new sample of bismuth was ordered, which consists of granules (Aldrich, >99.99%). These bismuth granules needed to be ground into a powder before they could be used to create Fluoride-ion batteries. The attempts to grind the bismuth granules are listed in table 24. Any action carried out under an inert atmosphere in this table is carried out in a MBRAUN UNIlab glovebox filled with 1 atm argon (Linde), with O_2 and H_2O concentrations of <10 ppm. Any ball-milling is done in a Fristch Pulverisette 7 Premium Line ball-milling machine. Any argon used in this table is from Linde.

From this table we found a method to grind bismuth into a powder suitable for producing fluoride-ion batteries. This powder was analyzed using X-ray Diffraction to check its oxygen content. From sample JZ-Bi-02, roughly 200 mg was placed in an airtight sample holder under an inert atmosphere. Then it was scanned in a PANanalytical X'Pert pro TTK-450 X-ray Diffractometer and measured for 29 minutes at angle 2θ=10-90. The results are shown in figure 50.

Sample number	**Method**	**Result**
JZ-Bi-01	Granules placed in ball-milling jar, filled with air. 2.2 g milled for 14 cycles of 10 minutes each at 100 rpm. Jar opened to check after every cycle.	No change was seen in the shape or size of the granules. During the first few cycles, the white ZrO_2 balls and the walls of the ball-milling jar showed a slight change in coloration, becoming darker, but no powder could be scraped off of either.
JZ-Bi-02	1 g of granules ground in a pestle and mortar in air into a coarse powder. This was placed in a ball-milling jar with 40 g ZrO_2 balls and milled for 6 cycles of 10 minutes, with 2 minute rests at 100 rpm.	The milling produced a fine powder with a dull gray color.
JZ-Bi-03	1.1 g of granules was ground by hand under an inert atmosphere. It was placed in a ball-milling jar with 20 g ZrO_2 balls, which was filled with argon ($\sim$1 atm). It was milled for 85 cycles of 10 minutes, with 2 minutes rest at 100 rpm.	The result were light gray granules of roughly the same size as previously. Possibly due to the high energy introduced during milling, the temperature rose and the bismuth had reached temperatures near or over its melting point, reforming granules.
JZ-Bi-04	1.0 g of granules were ground in a pestle and mortar under an inert atmosphere into a coarse powder. It was milled with 19 g of ZrO_2 balls for 12 cycles of 8 minutes with 2 minutes rests at 600 rpm under argon.	The coarse powder had resulted in a few intact (or reformed) granules and some loose powder, some of which had to be scraped off the wall and the ZrO_2 balls. The sample could be passed through a sieve to receive a fine powder, with a dark gray coloration and a metallic shine.
JZ-Bi-05	0.5 g of granules were hand ground into a coarse powder under an inert atmosphere. They were added to a ball-milling jar with 20 g of ZrO_2 balls and were milled under argon for 6 cycles of 8 minutes with 2 minutes rest at 100 rpm.	The result was a fine powder with a dull light gray coloration.

Table 24: Table listing the attempts to grind bismuth granules into a fine powder so that it can be used as part of the cathodic material in symmetric bismuth/bismuth fluoride batteries

From figure 50 we find that the bismuth powder contains no significant amount of oxygen. For example, the peak at 33° which was present in figure 49 and indicative of a Bi_2O_3 phase, is no longer present in this scan. The graph shows a single phase material. This material was therefore considered suitable for producing fluoride-ion batteries.

4.7 Second battery attempt

4.7.1 Production of new batteries

Next, the new, pure materials were tested to be used in new symmetrical batteries. New composite electrode material was made according to the steps outlined in section 3.6. The composition of the electrode is shown in table 25. Using this composite electrode, a battery was produced using the method in section 3.6, with the full composition of the battery shown in table 26.

Material	Cathodic compound 1	Cathodic compound 2
$BaSnF_4$ PG-100-7	114.0 mg	102.8 mg
BiF_3 (ApolloScientific, 99.99%)	51.4 mg	44.8 mg
Bi (JZ-Bi-5)	36.2 mg	34.3 mg
Carbon nanofiber (Aldrich)	12.0 mg	10.3 mg
Carbon black (Cabot)	10.5 mg	11.3 mg

Table 25: Components of cathodic compounds used to make the second batch of symmetrical fluoride-ion batteries

Battery	Cathodic compound	Weight cathode top	Weight electrolyte	Weight cathode bottom
1	1	13.8 mg	235.5 mg	29.6 mg
2	1	13.3 mg	195.0 mg	44.5 mg
3	2	12.4 mg	215.2 mg	30.4 mg
4	2	15.6 mg	197.9 mg	31.1 mg

Table 26: Components added to each of the new fluoride-ion batteries

4.7.2 Testing of new batteries

Each of the batteries was removed from the glovebox and connected to a MACCOR 4000a Automated Test System, where it had a constant current of 45 μA (57 μA cm^{-2}) applied to it until it reached 1 V, and then had a current of -45 μA (-57 μA cm^{-2}) applied to it until it reached -1 V, which would be repeated for 10 cycles. The second battery ran into an error and the measurement did not complete. For the others, the capacity of each cycle is plotted against the voltage in figures 51, 52 and 53. In these graphs it should be noted that the batteries were constructed such that at the start of the experiment, the composition of the electrode on both sides was identical, and thus the battery was exactly halfway between the charged and discharged state. This is why the first charge cycle shows a lower capacity than the first discharge cycle or the second charge cycle.

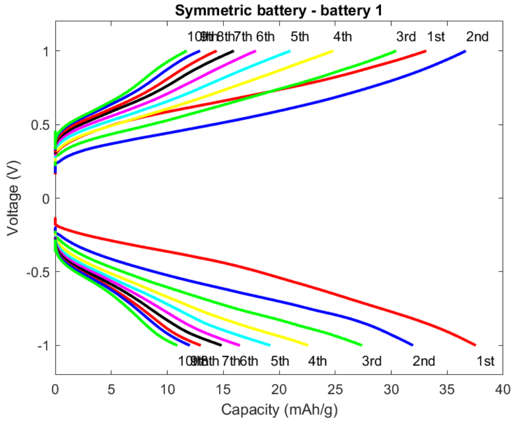

Figure 51: Capacity of the first battery during 10 charge-discharge cycles

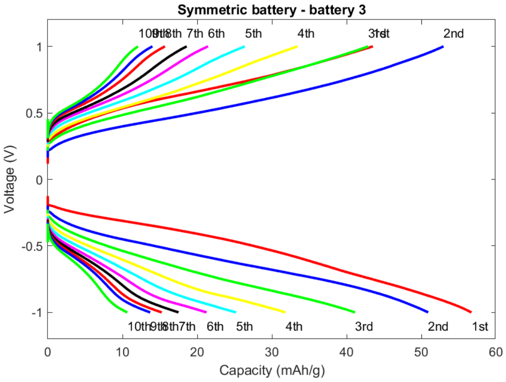

Figure 52: Capacity of the third battery during 10 charge-discharge cycles

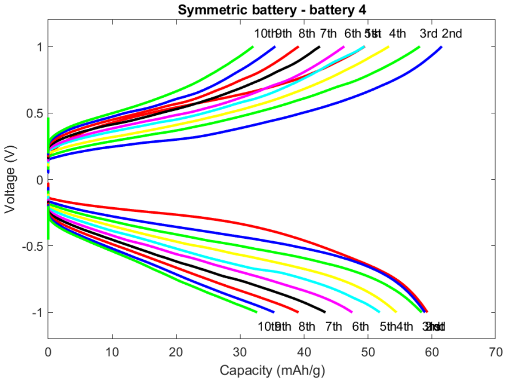

Figure 53: Capacity of the fourth battery during 10 charge-discharge cycles

From these graphs, it can be noted that there is a clear difference in performance between the three batteries. The third and fourth battery clearly have the best performance, with the first three cycles showing a capacity of around 60 mAh/g for the fourth battery, and having a capacity of over 30 mAh/g even after 10 cycles. The third performs slightly worse in the first few cycles, with a capacity of around 50 mAh/g, and has much worse capacity retention, going down to 10 mAh/g in the last few cycles. The first battery performs even worse, reaching only around 35 mAh/g in the first few cycles, and quickly decaying to around 10 mAh/g in subsequent cycles. One possible explanation for this difference is the thickness of the electrolyte. The fourth battery had the thinnest electrolyte, and thus the lowest resistance, whereas the first battery had the thickest electrolyte and thus the highest resistance. It is also noteworthy that the fourth battery has a lower overpotential than either of the others, and has a better capacity retention. It is possible that those two factors are linked.

It should also be noted that the capacities found here for the best performing battery, battery 4, were only around 30% of the values reported in literature[27]. These batteries are still underperforming other batteries that were reported on.

4.8 Tin-doped batteries

4.8.1 Production of tin-doped batteries

Now that the batteries from literature have been reproduced, albeit with lower capacities, another attempt to produce fluoride-ion batteries was carried out, this time with tin-doped bismuth fluoride. The hypothesis here was that the doping of the bismuth fluoride, which leads to higher ionic conductivity, as seen in section 4.5, would improve the battery characteristics.

For these experiments, new tin-doped BiF_3 samples containing 5% SnF_2 and 10% SnF_2 were produced using the steps described in section 3.4. Their ionic conductivity was tested using the procedure in section 3.7. The results are given in table 27 and depicted in figure 54 and 55. The pure BiF_3 sample from section 4.5.3 is also shown as a comparison. As can be seen in this graph, the ionic conductivity of BiF_3 was significantly improved through the doping with SnF_2. The value for the 10% SnF_2 doped material, with an ionic conductivity of 0.0147 mS cm^{-1} is comparable to the value found in section 4.5.3, where 10% SnF_2-doped BiF_3 had an ionic conductivity of 0.0185 mS cm^{-1}. These samples were used to produce composite electrolytes, with the ratios of each material listed in table 28.

Material	x_1/mm	x_2/mm	x_3/mm	x_4/mm	x_5	x_{av}/mm	Resistance	Conductivity
BiF_3	0.552	0.556	0.581	0.586	0.596	0.5762	19584	0.00375 mS cm^{-1}
BiF_3 with 5% SnF_2	0.695	0.656	0.715	0.604	0.628	0.6594	13179	0.00637 mS cm^{-1}
BiF_3 with 10% SnF_2	0.578	0.692	0.723	0.631	0.654	0.6556	5688	0.0147 mS cm^{-1}

Table 27: Results from the impedance measurement of the tin-doped BiF_3 materials used to produce batteries

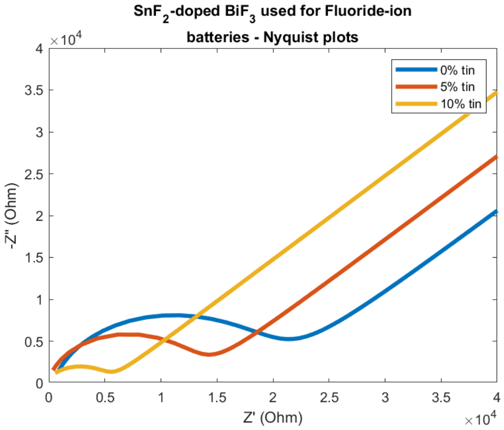

Figure 54: Nyquist plots of the tin-doped BiF_3 materials used to produce batteries

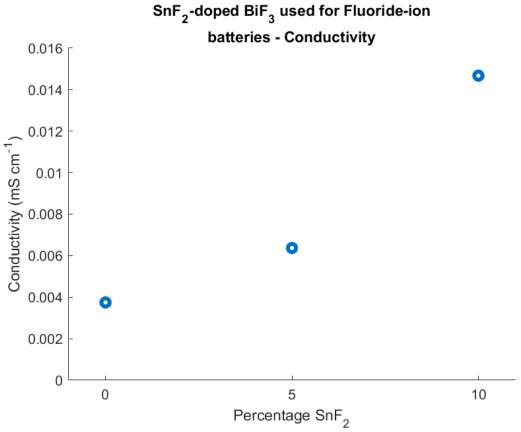

Figure 55: Resistances of the tin-doped BiF_3 materials used to produce batteries

Material	**Cathodic compound 5% tin**	**Cathodic compound 10% tin**
$BaSnF_4$	108.1 mg	107.7 mg
Doped BiF_3	47.4 mg	43.4 mg
Bi (JZ-Bi-5)	34.6 mg	33.5 mg
Carbon nanofiber (Aldrich)	10.3 mg	9.1 mg
Carbon black (Cabot)	10.4 mg	9.3 mg

Table 28: Components of cathodic compounds used to make the batch of doped symmetrical fluoride-ion batteries

Subsequently, these electrode compounds were used to produce two batteries each according to the steps set out in section 3.6. The precise weights of the electrolyte and cathodic compounds used are listed in table 29.

Battery	Doping type	Weight electrode top	Weight electrolyte	Weight electrode bottom
1	5%	15.0 mg	184.6 mg	32.1 mg
2	5%	16.5 mg	195.0 mg	41.2 mg
3	10%	17.8 mg	176.2 mg	37.0 mg
4	10%	22.1 mg	182.2 mg	41.6 mg

Table 29: Components added to each of the new fluoride-ion batteries

4.8.2 Testing of tin-doped batteries

Each of the batteries was removed from the glovebox and connected to a MACCOR 4000a Automated Test System, where it had a constant current of 45 μA (57 μA cm^{-2}) applied to it until it reached 1 V, and then had a current of -45 μA (-57 μA cm^{-2}) applied to it until it reached -1 V, which would be repeated for 10 cycles. The first and third battery ran into an error and the measurement did not complete. For the other two, the capacity of each cycle is plotted against the voltage in figures 56, and 57. Again, it should be noted that the batteries were constructed such that at the start of the experiment, the composition of the electrode on both sides was identical, and thus the battery was exactly halfway between the charged and discharged state. This is why the first charge cycle shows a lower capacity than the first discharge cycle or the second charge cycle.

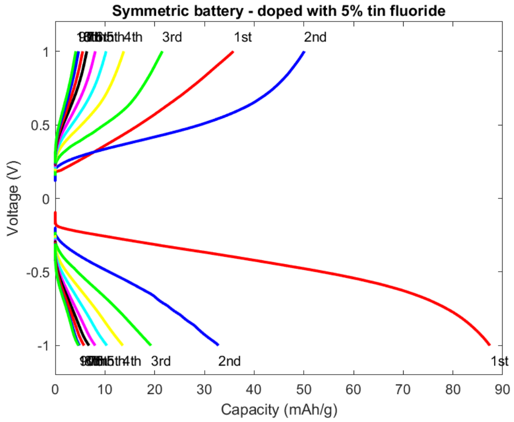

Figure 56: Capacity of the battery doped with 5% tin fluoride during 10 charge-discharge cycles

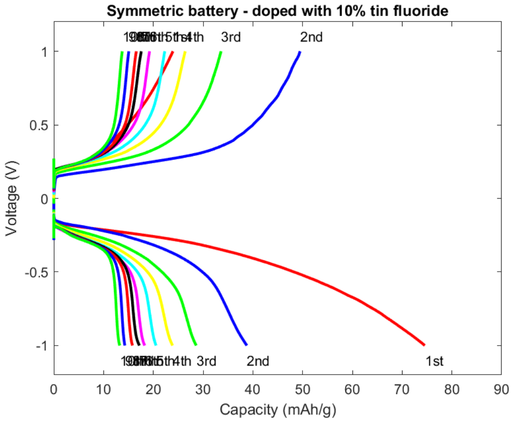

Figure 57: Capacity of the battery doped with 10% tin fluoride during 10 charge-discharge cycles

From the figures above, we can see that compared to the non-doped batteries, the initial cycles show a comparable capacity to the third and fourth non-doped battery, with the battery doped with 10% tin fluoride having a large discharge capacity in the first cycle. However, the capacity retention appears to be lower in the tin-doped batteries than in the non-doped batteries, with the battery doped with 10% tin fluoride reaching capacities of around 15 mAh/g after 10 cycles, and the battery doped with 5% tin fluoride reaching capacities of around 5 mAh/g after 10 cycles. The graph in figure 58 shows the behaviour of these batteries compared to the undoped batteries.

Besides the change in capacity, another interesting aspect in these graphs is the change in shape. In figure 51, 52 and 53, the voltage increases and decreases linearly with the time. This does not mirror the shape of the graph in figure 19, where at the voltage where the reaction occurs, a voltage plateau occurs, where the voltage remains roughly constant. This is because for these graphs, the applied current density is likely above the critical current density, and therefore diffusion effects dominate. In figure 57 the plateau is clearly present for all cycles. In figure 56, it is present for the first cycle and

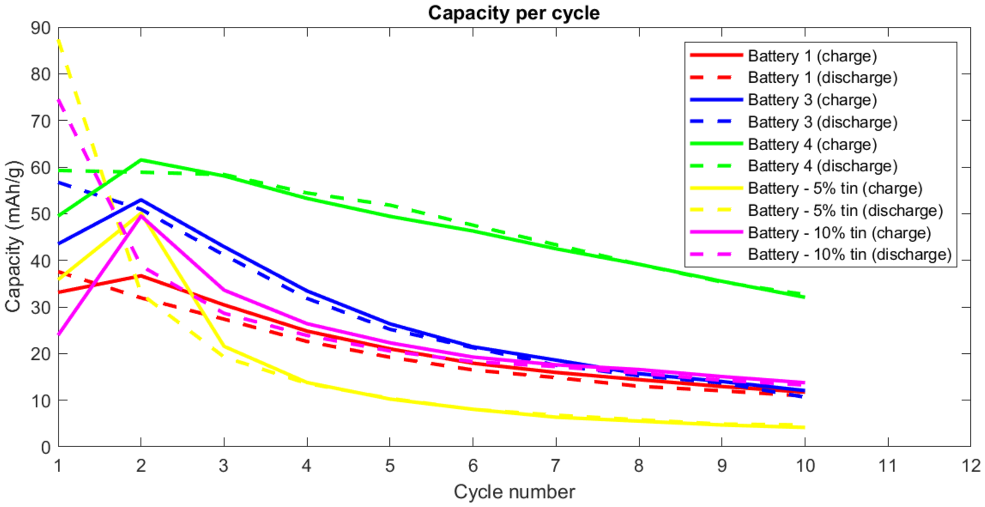

Figure 58: Charge and discharge capacity for each battery during the 10 cycles

the second charge cycle but not for the rest of the cycles.

The current density that was used, 57 μA cm^{-2}, was higher than values used in literature. This was done due to equipment constraints, as the MACCOR 4000a battery tester that was used was prone to running into errors at lower currents. For the batteries with undoped electrodes, it is likely that this current was above the critical current density and therefore no voltage plateaus are visible. For the battery whose electrode was doped with 5% SnF_2, a voltage plateau is visible in the first few cycles, so it is likely that the critical current density was not reached in these cycles. In later cycles, no voltage plateau is visible, so likely the critical current density went down (possibly due to a decrease in the ionic conductivity of the electrode material due to structural changes) and now the applied current density is above the critical current density. For the battery whose electrode was doped with 10% SnF_2, a voltage plateau is visible in all cycles. Thus, it can be concluded that doping the BiF_3 electrode material with SnF_2 increases the critical current density, which allows the battery to be charged and discharged at higher current densities, thus increasing the power output.

5 Conclusion

In this thesis it was attempted to produce a working $BiF_3; Bi|BaSnF_4|Bi; BiF_3$ symmetrical fluoride-ion battery such as reported by Grenier [27]. During the first attempt to build this battery, no significant capacity was measured.

Two hypotheses were provided for the failure of this battery to provide a significant capacity. One was that the loss of pressure after pressing the battery pellet caused the ionic conductivity to decrease. The other was that impurities in the materials used to synthesize the battery decreased the ionic conductivity.

Both these hypotheses were tested. First, the effect of pressure on the cell was measured. Both the electrolyte material $\mathrm{BaSnF_4}$ and the electrode material $\mathrm{BiF_3}$ were tested for the effect the pressure had on their ionic conductivity. $\mathrm{BaSnF_4}$ reached a maximum ionic conductivity at a pressure of ∼280 MPa whereas $\mathrm{BiF_3}$ reached a maximum ionic conductivity at a pressure of ∼680 MPa. The latter specifically was significantly lower than the pressure that was applied during production, which was usually around 240 MPa. This was reasoned to have contributed to the lack of performance by the battery. Another interesting finding was that the ionic conductivity increased along the increasing pressure in two steps for both materials, which is very different to the conductivity behaviour at different pressures for other materials listed in literature. Reasons for this behaviour could not be deduced from the experiments, but could be worth looking into.

Next, the materials used to produce the battery were tested for impurities. Since all materials were sensitive to oxygen, special focus was placed on trying to find oxide impurities. The electrolyte material $\mathrm{BaSnF_4}$ was found to be relatively pure, but the electrode materials $\mathrm{BiF_3}$ and Bi-powder were found to have significant oxygen impurities.

Thereafter, it was analyzed whether oxygen impurities indeed have an adverse effect on the ionic conductivity of $\mathrm{BiF_3}$. Different Bi-O-F compounds were synthesized with different amounts of oxide contents. The materials had their ionic conductivity measured, and it was found that all oxide-containing materials had a drastically lower ionic conductivity (by a factor 1,000 to 10,000) than the pure $\mathrm{BiF_3}$ material. Since $\mathrm{BiF_3}$ is sensitive to oxygen and humidity, and is prone to forming oxides when in contact with either, this was hypothesized to be one of the reasons why the batteries in the first attempt failed to give a significant capacity.

To test whether the electrode conductivity could be improved by doping $\mathrm{BiF_3}$, $\mathrm{BiF_3}$ was doped with different amounts of $\mathrm{SnF_2}$, for which the group of Pei showed using first-principle calculations that it could improve the ionic conductivity of the material[95]. Materials with tin concentration from 10-20% were synthesized and had their ionic conductivity measured. It was found that $\mathrm{BiF_3}$ doped with 10% $\mathrm{SnF_2}$ increased the ionic conductivity of $\mathrm{BiF_3}$ by a factor 5, while doping with 15% and 20% $\mathrm{SnF_2}$ lead to an ionic conductivity comparable to that of pure $\mathrm{BiF_3}$.

A new source of $\mathrm{BiF_3}$ was then acquired and was found to have almost no oxide impurities, and bismuth granules were manually ground to make a bismuth powder with also no oxide impurities. These materials were used to create a new batch of symmetrical fluoride-ion batteries. Four batteries were made, of which three succesfully ran and produced a capacity. This capacity was roughly 30% of the values reported by Grenier [27], and they fluctuated somewhat, though this was hypothesized to partially be caused by differences in the thickness of the electrolyte pellet.

Lastly, two new batteries were created, which both had doped $\mathrm{BiF_3}$ as electrode material, with one being doped with 5% $\mathrm{SnF_2}$ and one being doped with 10% $\mathrm{SnF_2}$. These batteries showed a higher initial capacity than the non-doped batteries, but had a higher capacity decay as well. The small sample size and the random fluctuations between similar batteries make it harder to draw definitive conclusions on this, but these seemed to be the general trends. Another finding was that the critical current density of the electrode materials had increased as a consequence of doping with $\mathrm{SnF_2}$, which allows higher current densities to be applied to the batteries, increasing their power output.

To conclude, the material composition and ionic conductivity of the electrolyte and electrode material play a huge role on the characteristics of fluoride-ion batteries. Adjusting these material properties using doping could be an important road to improving on the fluoride-ion battery performance.

References

[1] M. M. Ahmad, Y. Yamane, and K. Yamada. Structure, ionic conduction, and giant dielectric properties of mechanochemically synthesized $BaSnF_4$. *Journal of Applied Physics*, 106(7):074106, Oct. 2009.

[2] E. S. Ameh. A review of basic crystallography and x-ray diffraction applications. *The International Journal of Advanced Manufacturing Technology*, 105(7-8):3289–3302, Nov. 2019.

[3] D. R. Askeland and P. Webster. *The Science and Engineering of Materials.* Chapman and Hall, 1990.

[4] B. Aurivillius, C. Brosset, T. Ledaal, and H. M. Seip. The crystal structure of bismuth oxide fluoride. II. a refinement of the previously published structure. *Acta Chemica Scandinavica*, 18:1823–1830, 1964.

[5] B. Aurivillius and T. Lundqvist. Xray studies on the system BiF_3-Bi_2O_3. *Acta Chem. Scand.*, 9(7):1209–1212, 1955.

[6] E. Bastow. The 6 alloy families: Bismuth. `https://www.indium.com/blog/the-6-alloy-families-bismuth.php#:~:text=Bismuth%20also%20readily%20alloys%20with,a%20lot%20in%20fire%20suppression.` *Indium Corporation*, 2016.

[7] Battery University. BU-402: What Is C-rate? `https://batteryuniversity.com/article/bu-402-what-is-c-rate`, 2021.

[8] W. Baukal. Über reaktionsmöglichkeiten in elektroden von festkörperbatterien. *Electrochimica Acta*, 19(11):687–694, Nov. 1974.

[9] J. F. Baumgärtner, F. Krumeich, M. Wörle, K. V. Kravchyk, and M. V. Kovalenko. Thermal synthesis of conversion-type bismuth fluoride cathodes for high-energy-density Li-ion batteries. *Communications Chemistry*, 5(1), Jan. 2022.

[10] S. Bromberg and K. Dill. *Molecular Driving Forces: Statistical Thermodynamics in Chemistry and Biology.* Garland Science, 2002.

[11] S. Chaudhuri, F. Wang, and C. P. Grey. Resolving the different dynamics of the fluorine sublattices in the anionic conductor $BaSnF_4$ by using high-resolution MAS NMR techniques. *Journal of the American Chemical Society*, 124(39):11746–11757, Sept. 2002.

[12] Y. Chen, Y. Kang, Y. Zhao, L. Wang, J. Liu, Y. Li, Z. Liang, X. He, X. Li, N. Tavajohi, and B. Li. A review of lithium-ion battery safety concerns: The issues, strategies, and testing standards. *Journal of Energy Chemistry*, 59:83–99, Aug. 2021.

[13] China Energy Storage Alliance. CNESA Global Energy Storage Market Analysis – 2020.Q1 (Summary). `http://en.cnesa.org/latest-news/2020/5/28/cnesa-global-energy-storage-market-analysis-2020q1-summary`, 2020.

[14] M. Cronau, M. Szabo, C. König, T. B. Wassermann, and B. Roling. How to measure a reliable ionic conductivity? the stack pressure dilemma of microcrystalline sulfide-based solid electrolytes. *ACS Energy Letters*, 6(9):3072–3077, Aug. 2021.

[15] M. Dailey. What makes lithium batteries so expensive? `https://www.energyandcapital.com/articles/what-makes-lithium-batteries-so-expensive-/77136`. *Energy & Capital*, 2017.

[16] Y. Danto, G. Poujade, J. Pistré, C. Lucat, and J. Salardenne. A Pb|PbF2|BiF3|Bi thin solid film reversible galvanic cell. *Thin Solid Films*, 55(3):347–354, Dec. 1978.

[17] D. Devaux, H. Leduc, P. Dumaz, M. Lecuyer, M. Deschamps, and R. Bouchet. Effect of electrode and electrolyte thicknesses on all-solid-state battery performance analyzed with the sand equation. *Frontiers in Energy Research*, 7, Jan. 2020.

[18] J.-M. Doux, Y. Yang, D. H. S. Tan, H. Nguyen, E. A. Wu, X. Wang, A. Banerjee, and Y. S. Meng. Pressure effects on sulfide electrolytes for all solid-state batteries. *Journal of Materials Chemistry A*, 8(10):5049–5055, 2020.

[19] S. Elzwawi. *Cathodic Arc Zinc Oxide for Active Electronic Devices.* PhD thesis, 02 2015.

[20] T. Famprikis, O. U. Kudu, J. A. Dawson, P. Canepa, F. Fauth, E. Suard, M. Zbiri, D. Dambournet, O. J. Borkiewicz, H. Bouyanfif, S. P. Emge, S. Cretu, J.-N. Chotard, C. P. Grey, W. G. Zeier, M. S. Islam, and C. Masquelier. Under pressure: Mechanochemical effects on structure and ion conduction in the sodium-ion solid electrolyte Na_3PS_4. *Journal of the American Chemical Society*, 142(43):18422–18436, Oct. 2020.

[21] F. Flatscher, M. Philipp, S. Ganschow, H. M. R. Wilkening, and D. Rettenwander. The natural critical current density limit for $Li_7La_3Zr_2O_{12}$ garnets. *Journal of Materials Chemistry A*, 8(31):15782–15788, 2020.

[22] M. S. Frant and J. W. Ross. Electrode for sensing fluoride ion activity in solution. *Science*, 154(3756):1553–1555, Dec. 1966.

[23] G. B. Haxel, J. B. Hedrick, G. J. Orris. Rare earth elements—critical resources for high technology. https://pubs.usgs.gov/fs/2002/fs087-02/. *US geological survey*, 2005.

[24] J. Gerdes. The role of battery storage in the energy transition. https://www.energymonitor.ai/tech/energy-storage/the-role-of-battery-storage-in-the-energy-transition. *Energy monitor*, 2021.

[25] M. Ghiji, V. Novozhilov, K. Moinuddin, P. Joseph, I. Burch, B. Suendermann, and G. Gamble. A review of lithium-ion battery fire suppression. *Energies*, 13(19):5117, Oct. 2020.

[26] P. Greim, A. A. Solomon, and C. Breyer. Assessment of lithium criticality in the global energy transition and addressing policy gaps in transportation. *Nature Communications*, 11(1), Sept. 2020.

[27] A. Grenier, A. G. P. Gutierrez, H. Groult, and D. Dambournet. Modified coin cells to evaluate the electrochemical properties of solid-state fluoride-ion batteries at 150 °C. *Journal of Fluorine Chemistry*, 191:23–28, Nov. 2016.

[28] A. Grenier, A.-G. Porras-Gutierrez, H. Groult, K. A. Beyer, O. J. Borkiewicz, K. W. Chapman, and D. Dambournet. Electrochemical reactions in fluoride-ion batteries: mechanistic insights from pair distribution function analysis. *Journal of Materials Chemistry A*, 5(30):15700–15705, 2017.

[29] R. J. Gummow, G. Vamvounis, M. B. Kannan, and Y. He. Calcium-ion batteries: Current state-of-the-art and future perspectives. *Advanced Materials*, 30(39):1801702, July 2018.

[30] B. Heligman. Galvanostatic cycling. https://science-research.fandom.com/wiki/Galvanostatic_Cycling. *Science research wiki*, 2019.

[31] B. Hu, X. Wang, H. Shu, X. Yang, L. Liu, Y. Song, Q. Wei, H. Hu, H. Wu, L. Jiang, and X. Liu. Improved electrochemical properties of BiF_3/c cathode via adding amorphous $AlPO_4$ for lithium-ion batteries. *Electrochimica Acta*, 102:8–18, July 2013.

[32] R. A. Huggins. *Advanced Batteries: Material Science Aspects.* Springer, 1^{st} edition, 2009.

[33] J.-Y. Hwang, S.-T. Myung, and Y.-K. Sun. Sodium-ion batteries: present and future. *Chemical Society Reviews*, 46(12):3529–3614, 2017.

[34] International Energy Agency. A rapid rise in battery innovation is playing a key role in clean energy transitions. https://www.iea.org/news/a-rapid-rise-in-battery-innovation-is-playing-a-key-role-in-clean-energy-transitions, 2020.

[35] International Energy Agency. The role of critical minerals in clean energy transitions. https://www.iea.org/reports/the-role-of-critical-minerals-in-clean-energy-transitions, 2021.

[36] B. Ji, H. He, W. Yao, and Y. Tang. Recent advances and perspectives on calcium-ion storage: Key materials and devices. *Advanced Materials*, 33(2):2005501, Nov. 2020.

[37] A. Kalair, N. Abas, M. S. Saleem, A. R. Kalair, and N. Khan. Role of energy storage systems in energy transition from fossil fuels to renewables. *Energy Storage*, 3(1), Feb. 2020.

[38] J. H. Kennedy and J. C. Hunter. Thin-film galvanic cell Pb / PbF2 / PbF2 , CuF2 / Cu. *Journal of The Electrochemical Society*, 123(1):10–14, Jan. 1976.

[39] J. H. Kennedy and R. C. Miles. Ionic conductivity of doped beta-lead fluoride. *Journal of The Electrochemical Society*, 123(1):47–51, Jan. 1976.

[40] M. Kocher, A. Jain, S. P. Ong, and G. Hautier. mp-685136: BiF_3 (hexagonal, $P6_3/mmc$, 194). https://materialsproject.org/materials/mp-685136/. *Materials Project*, 2020.

[41] H. Konishi, T. Minato, T. Abe, and Z. Ogumi. Difference of rate performance between discharge and charge reactions for bismuth fluoride electrode in lithium-ion battery. *Journal of Electroanalytical Chemistry*, 806:82–87, Dec. 2017.

[42] H. Konishi, T. Minato, T. Abe, and Z. Ogumi. Electrochemical performance of BiF_3-BaF_2 solid solution with three different phases on a fluoride shuttle battery system. *ChemistrySelect*, 5(16):4943–4946, Apr. 2020.

[43] T. Krauskopf, H. Hartmann, W. G. Zeier, and J. Janek. Toward a fundamental understanding of the lithium metal anode in solid-state batteries—an electrochemo-mechanical study on the garnet-type solid electrolyte $Li_{6.25}Al_{0.25}La_3Zr_2O_{12}$. *ACS Applied Materials &amp Interfaces*, 11(15):14463–14477, Mar. 2019.

[44] P. P. Kumar and S. Yashonath. Ionic conduction in the solid state. *Journal of Chemical Sciences*, 118(1):135–154, Jan. 2006.

[45] M. Lacey. The principles of electrochemical impedance spectroscopy. http://lacey.se/science/eis/eis-principles/. *Battery science and electrochemistry*, 2018.

[46] J. Laval, J. Champarnaud-Mesjard, B. Frit, A. Britel, and A. Mikou. $Bi_7O_5F_{11}$: a new ordered anion-excess fluorite-related structure with columnar clusters. *European Journal of Solid State Inorganic Chemistry*, 31:943–956, 1994.

[47] K.-S. Lee, S.-T. Myung, K. Amine, H. Yashiro, and Y.-K. Sun. Dual functioned BiOF-coated li$[Li_{0.1}Al_{0.05}Mn_{1.85}]O_4$ for lithium batteries. *Journal of Materials Chemistry*, 19(14):1995, 2009.

[48] J. M. Leger, J. Haines, A. Atouf, O. Schulte, and S. Hull. High-pressure x-ray- and neutron-diffraction studies of BaF_2: An example of a coordination number of 11 in AX2 compounds. 52(18):13247–13256, 1995.

[49] D. Li, Y. Yuan, J. Liu, M. Fichtner, and F. Pan. A review on current anode materials for rechargeable Mg batteries. *Journal of Magnesium and Alloys*, 8(4):963–979, Dec. 2020.

[50] D. R. Lide. *CRC Handbook of Chemistry and Physics - 89th edition*. Taylor Francis, 2008.

[51] L. Liu, L. Yang, D. Shao, K. Luo, C. Zou, Z. Luo, and X. Wang. Nd_3 doped $BaSnF_4$ solid electrolyte for advanced room-temperature solid-state fluoride ion batteries. *Ceramics International*, 46(12):20521–20528, Aug. 2020.

[52] B. V. Lotsch and J. Maier. Relevance of solid electrolytes for lithium-based batteries: A realistic view. *Journal of Electroceramics*, 38(2-4):128–141, June 2017.

[53] G. Malmros, L. Fernholt, C. J. Ballhausen, U. Ragnarsson, S. E. Rasmussen, E. Sunde, and N. A. Sørensen. The crystal structure of alpha-Bi_2O_2. *Acta Chemica Scandinavica*, 24:384–396, 1970.

[54] M. Mansmann. Die kristall struktur von lanthantrifluorid. *Zeitschrift für Kristallographie - Crystalline Materials*, 122(1-6):375–398, Dec. 1965.

[55] J. Markard. The next phase of the energy transition and its implications for research and policy. *Nature Energy*, 3(8):628–633, May 2018.

[56] A. Masias, N. Felten, R. Garcia-Mendez, J. Wolfenstine, and J. Sakamoto. Elastic, plastic, and creep mechanical properties of lithium metal. *Journal of Materials Science*, 54(3):2585–2600, Oct. 2018.

[57] Materials project. mp-23237: BiF_3 (orthorhombic, Pnma, 62). `https://materialsproject.org/materials/mp-23237/`. *Materials project*, 2020.

[58] Materials project. mp-23301: BiF_3 (cubic, fm-3m, 225). `https://materialsproject.org/materials/mp-23301/`. *Materials project*, 2020.

[59] Z. Melhem. *Electricity transmission, distribution and storage systems.* Woodhead Publishing, Oxford, 2013.

[60] Minerals Education Coaltion. Fluorine. `https://mineralseducationcoalition.org/elements/fluorine/`, n.d.

[61] I. Mohammad, R. Witter, M. Fichtner, and M. A. Reddy. Room-temperature, rechargeable solid-state fluoride-ion batteries. *ACS Applied Energy Materials*, 1(9):4766–4775, Aug. 2018.

[62] R. Murugan, V. Thangadurai, and W. Weppner. Fast lithium ion conduction in garnet-type $Li_7La_3Zr_2O_{12}$. *Angewandte Chemie International Edition*, 46(41):7778–7781, Oct. 2007.

[63] R. Nave. Single slit diffraction intensity. `http://hyperphysics.phy-astr.gsu.edu/hbase/phyopt/mulslid.html`. *HyperPhysics*, n.d.

[64] D. A. Neaman. *Semiconductor Physics and Devices - Basic principles.* McGraw-Hill Higher Education, 3^{rd} edition, 2003.

[65] M. A. Nowroozi, I. Mohammad, P. Molaiyan, K. Wissel, A. R. Munnangi, and O. Clemens. Fluoride ion batteries – past, present, and future. *Journal of Materials Chemistry A*, 9(10):5980–6012, 2021.

[66] PalmSens Knowledge Base. Electrochemical impedance spectroscopy (eis). `https://www.palmsens.com/knowledgebase-article/electrochemical-impedance-spectroscopy-eis/`, n.d.

[67] S. Prakash. Why lithium-ion batteries are so expensive? `https://newspatrolling.com/why-lithium-ion-batteries-are-so-expensive/#:~:text=Expensive%20metals%20%E2%80%93%20Lithium%2Dion%20battery,metals%20like%20iron%20or%20aluminum.` *News patrolling*, 2021.

[68] F. Preishuber-Pflügl, V. Epp, S. Nakhal, M. Lerch, and M. Wilkening. Defect-enhanced F^- ion conductivity in layer-structured nanocrystalline BaSnF4 prepared by high-energy ball milling combined with soft annealing. *physica status solidi (c)*, 12(1-2):10–14, Nov. 2014.

[69] E. Quartarone and P. Mustarelli. Review—emerging trends in the design of electrolytes for lithium and post-lithium batteries. *Journal of The Electrochemical Society*, 167(5):050508, Jan. 2020.

[70] M. Rahm, R. Hoffmann, and N. W. Ashcroft. Atomic and ionic radii of elements 1 –96. *Chemistry – A European Journal*, 22(41):14625–14632, Aug. 2016.

[71] E. P. Randviir and C. E. Banks. Electrochemical impedance spectroscopy: an overview of bioanalytical applications. *Analytical Methods*, 5(5):1098, 2013.

[72] M. A. Reddy and M. Fichtner. Batteries based on fluoride shuttle. *Journal of Materials Chemistry*, 21(43):17059, 2011.

[73] H. Ribeiro and M. Yuen. Infographic: Insufficient lithium supply could decelerate energy transition. https://www.spglobal.com/platts/en/market-insights/latest-news/metals/012622-infographic-the-lithium-deficit-road-map-will-future-supply-meet-demand. *SP Global Platts*, 2022.

[74] A. Roos and J. Schoonman. Electronic conductivity in $La_{1-x}Ba_xF_{3-x}$ crystals. *Solid State Ionics*, 13(3):205–211, June 1984.

[75] Y. Saito, W. Morimura, R. Kuratani, and S. Nishikawa. Factors controlling the ionic mobility of lithium electrolyte solutions in separator membranes. *The Journal of Physical Chemistry C*, 120(7):3619–3624, Feb. 2016.

[76] K. Shimoda, T. Minato, H. Konishi, G. Kano, T. Nakatani, S. Fujinami, A. C. Kucuk, S. Kawaguchi, Z. Ogumi, and T. Abe. Defluorination/fluorination mechanism of $Bi_{0.8}Ba_{0.2}F_{2.8}$ as a fluoride shuttle battery positive electrode. *Journal of Electroanalytical Chemistry*, 895:115508, Aug. 2021.

[77] SnapSolve. How does the doping increase the conductivity of semiconductors? https://www.snapsolve.com/class12/chemistry/cbse-1100309777, n.d.

[78] N. I. Sorokin, P. P. Fedorov, O. K. Nikol'skaya, O. A. Nikeeva, E. G. Rakov, and E. I. Ardashnikova. Electrical Properties of $PbSnF_4$ Materials Prepared by Different Methods. *Inorganic Materials*, 37(11):1178–1182, 2001.

[79] N. I. Sorokin and B. P. Sobolev. Nonstoichiometric fluorides—Solid electrolytes for electrochemical devices: A review. *Crystallography Reports*, 52(5):842–863, Sept. 2007.

[80] Z. Su, J. Liu, M. Li, Y. Zhu, S. Qian, M. Weng, J. Zheng, Y. Zhong, F. Pan, and S. Zhang. Defect engineering in titanium-based oxides for electrochemical energy storage devices. *Electrochemical Energy Reviews*, 3(2):286–343, Feb. 2020.

[81] T. Takahashi, H. Iwahara, and T. Ishikawa. Ionic conductivity of doped cerium trifluoride. *Journal of The Electrochemical Society*, 124(2):280–284, Feb. 1977.

[82] N. Tapia-Ruiz, A. R. Armstrong, H. Alptekin, M. A. Amores, H. Au, J. Barker, R. Boston, W. R. Brant, J. M. Brittain, Y. Chen, M. Chhowalla, Y.-S. Choi, S. I. R. Costa, M. C. Ribadeneyra, S. A. Cussen, E. J. Cussen, W. I. F. David, A. V. Desai, S. A. M. Dickson, E. I. Eweka, J. D. Forero-Saboya, C. P. Grey, J. M. Griffin, P. Gross, X. Hua, J. T. S. Irvine, P. Johansson, M. O. Jones, M. Karlsmo, E. Kendrick, E. Kim, O. V. Kolosov, Z. Li, S. F. L. Mertens, R. Mogensen, L. Monconduit, R. E. Morris, A. J. Naylor, S. Nikman, C. A. O'Keefe, D. M. C. Ould, R. G. Palgrave, P. Poizot, A. Ponrouch, S. Renault, E. M. Reynolds, A. Rudola, R. Sayers, D. O. Scanlon, S. Sen, V. R. Seymour, B. Silván, M. T. Sougrati, L. Stievano, G. S. Stone, C. I. Thomas, M.-M. Titirici, J. Tong, T. J. Wood, D. S. Wright, and R. Younesi. 2021 roadmap for sodium-ion batteries. *Journal of Physics: Energy*, 3(3):031503, July 2021.

[83] J.-M. Tarascon and M. Armand. Issues and challenges facing rechargeable lithium batteries. *Nature*, 414(6861):359–367, Nov. 2001.

[84] S. Thomspon. Storage is at the heart of the energy transition. https://www.theagilityeffect.com/en/opinions/storage-is-at-the-heart-of-the-energy-transition/. *The Agility Effect*, 2020.

[85] P. Vadhva, J. Hu, M. J. Johnson, R. Stocker, M. Braglia, D. J. L. Brett, and A. J. E. Rettie. Electrochemical impedance spectroscopy for all-solid-state batteries: Theory, methods and future outlook. *ChemElectroChem*, 8(11):1930–1947, May 2021.

[86] P. Villars. B-F-O vertical section of ternary phase diagram. 2016.

[87] M. A. Wahab. Unit cell representations of miller indices. In *Numerical Problems in Crystallography*, pages 137–178. Springer Singapore, 2021.

[88] M. J. Wang, R. Choudhury, and J. Sakamoto. Characterizing the Li-solid-electrolyte interface dynamics as a function of stack pressure and current density. *Joule*, 3(9):2165–2178, Sept. 2019.

[89] S. Wang, Y. Zhang, X. Zhang, T. Liu, Y.-H. Lin, Y. Shen, L. Li, and C.-W. Nan. High-conductivity argyrodite Li_6PS_5Cl solid electrolytes prepared via optimized sintering processes for all-solid-state lithium–sulfur batteries. *ACS Applied Materials & Interfaces*, 10(49):42279–42285, Nov. 2018.

[90] Y. Wang, R. Chen, T. Chen, H. Lv, G. Zhu, L. Ma, C. Wang, Z. Jin, and J. Liu. Emerging non-lithium ion batteries. *Energy Storage Materials*, 4:103–129, July 2016.

[91] J. Wood. Batteries are a key part of the energy transition. here's why. `https://www.weforum.org/agenda/2021/09/batteries-lithium-ion-energy-storage-circular-economy/#:~:text=Advances%20in%20battery%20technolog%20have,to%20help%20stabilise%20the%20grid.` *World Economic Forum*, 2021.

[92] G. Xu, Z. Liu, C. Zhang, G. Cui, and L. Chen. Strategies for improving the cyclability and thermo-stability of $LiMn_2O_4$-based batteries at elevated temperatures. *Journal of Materials Chemistry A*, 3(8):4092–4123, 2015.

[93] T. Yamanaka, K. ichi Okazaki, Z. Ogumi, and T. Abe. Reactivity and mechanisms in fluoride shuttle battery reactions: Difference between orthorhombic and cubic BiF_3 single microparticles. *ACS Applied Energy Materials*, 2(12):8801–8808, Nov. 2019.

[94] Z. Yan, B. Scott, S. L. Glazier, and M. N. Obrovac. Current-corrected cycling strategies for true electrode performance measurement. *Batteries & Supercaps*, 5(2), Dec. 2021.

[95] Z. Yang, S. Tan, Y. Huang, X. Wang, and Y. Pei. First-principles study on doping effect of Sn in BiF_3 as cathode materials for Li-ion battery. *Current Applied Physics*, 16(1):12–19, Jan. 2016.

[96] X. Yao, D. Liu, C. Wang, P. Long, G. Peng, Y.-S. Hu, H. Li, L. Chen, and X. Xu. High-energy all-solid-state lithium batteries with ultralong cycle life. *Nano Letters*, 16(11):7148–7154, Oct. 2016.

[97] S. E. Yoon, J. Park, J. E. Kwon, S. Y. Lee, J. M. Han, C. Y. Go, S. Choi, K. C. Kim, H. Seo, J. H. Kim, and B.-G. Kim. Improvement of electrical conductivity in conjugated polymers through cascade doping with small-molecular dopants. *Advanced Materials*, 32(49):2005129, Nov. 2020.

[98] S.-H. Yu, X. Feng, N. Zhang, J. Seok, and H. D. Abruña. Understanding conversion-type electrodes for lithium rechargeable batteries. *Accounts of Chemical Research*, 51(2):273–281, Jan. 2018.

[99] Y. Zhan, W. Zhang, B. Lei, H. Liu, and W. Li. Recent development of Mg ion solid electrolyte. *Frontiers in Chemistry*, 8, Feb. 2020.

[100] T. Zhao, H. Shu, Z. Shen, H. Hu, J. Wang, and X. Chen. Electrochemical lithiation mechanism of two-dimensional transition-metal dichalcogenide anode materials: Intercalation versus conversion reactions. *The Journal of Physical Chemistry C*, 123(4):2139–2146, Jan. 2019.